Monthly Notices
of the
ROYAL ASTRONOMICAL SOCIETY

MNRAS **442,** 2165–2187 (2014) doi:10.1093/mnras/stu771

The outer halo globular cluster system of M31 – I. The final PAndAS catalogue

A. P. Huxor,[1⋆] A. D. Mackey,[2] A. M. N. Ferguson,[3] M. J. Irwin,[4] N. F. Martin,[5] N. R. Tanvir,[6] J. Veljanoski,[3] A. McConnachie,[7] C. K. Fishlock,[2] R. Ibata[5] and G. F. Lewis[8]

[1]*Astronomisches Rechen-Institut, Zentrum für Astronomie der Universität Heidelberg, Mönchhofstraße 12 - 14, D-69120 Heidelberg, Germany*
[2]*Research School of Astronomy & Astrophysics, Australian National University, Mt Stromlo Observatory, Cotter Road, Weston Creek, ACT 2611, Australia*
[3]*SUPA, Institute for Astronomy, University of Edinburgh, Royal Observatory, Blackford Hill, Edinburgh EH9 3HJ, UK*
[4]*Institute of Astronomy, Madingley Road, Cambridge, CB3 0HA, UK*
[5]*Observatoire de Strasbourg, 11, rue de l'Université, F-67000 Strasbourg, France*
[6]*Department of Physics and Astronomy, University of Leicester, University Road, Leicester LE1 7RH, UK*
[7]*NRC Herzberg Institute of Astrophysics, 5071 West Saanich Road, Victoria, BC V9E 2E7, Canada*
[8]*Institute of Astronomy, School of Physics, A29, University of Sydney, NSW 2006, Australia*

Accepted 2014 April 16. Received 2014 April 16; in original form 2014 March 12

ABSTRACT

We report the discovery of 59 globular clusters (GCs) and two candidate GCs in a search of the halo of M31, primarily via visual inspection of Canada–France–Hawaii Telescope/MegaCam imagery from the Pan-Andromeda Archaeological Survey (PAndAS). The superior quality of these data also allows us to check the classification of remote objects in the Revised Bologna Catalogue (RBC), plus a subset of GC candidates drawn from Sloan Digital Sky Survey (SDSS) imaging. We identify three additional new GCs from the RBC, and confirm the GC nature of 11 SDSS objects (8 of which appear independently in our remote halo catalogue); the remaining 188 candidates across both lists are either foreground stars or background galaxies. Our new catalogue represents the first uniform census of GCs across the M31 halo – we find clusters to the limit of the PAndAS survey area at projected radii of up to $R_{\rm proj} \sim 150$ kpc. Tests using artificial clusters reveal that detection incompleteness cuts in at luminosities below $M_V = -6.0$; our 50 per cent completeness limit is $M_V \approx -4.1$. We construct a uniform set of PAndAS photometric measurements for all known GCs outside $R_{\rm proj} = 25$ kpc, and any new GCs within this radius. With these data, we update results from Huxor et al., investigating the luminosity function (LF), colours and effective radii of M31 GCs with a particular focus on the remote halo. We find that the GCLF is clearly bimodal in the outer halo ($R_{\rm proj} > 30$ kpc), with the secondary peak at $M_V \sim -5.5$. We argue that the GCs in this peak have most likely been accreted along with their host dwarf galaxies. Notwithstanding, we also find, as in previous surveys, a substantial number of GCs with above-average luminosity in the outer M31 halo – a population with no clear counterpart in the Milky Way.

Key words: galaxies: evolution – galaxies: haloes – galaxies: individual: M31 – galaxies: star clusters: general.

1 INTRODUCTION

Globular cluster (GC) systems are thought to trace both major star formation episodes and accretion events. As such they have proven to be valuable tools for the study of their host galaxies (Georgiev, Goudfrooij & Puzia 2012) – from the seminal Milky Way (MW) work of Searle & Zinn (1978) to recent studies of more distant galaxies (Chies-Santos et al. 2011; Forbes et al. 2011; Forte, Vega & Faifer 2012).

The GC system of M31 has naturally been the focus of particular interest, providing (as a massive spiral galaxy) an excellent comparison to our own MW. Moreover, the proximity of M31 (at ∼780 kpc)[1] allows for detailed investigation of its GC populations, which have been extensively studied (e.g. Crampton et al. 1985;

⋆E-mail: avon@ari.uni-heidelberg.de

[1] Throughout this paper, we use the distance to M31 from McConnachie et al. (2005); see also Conn et al. (2012).

Battistini et al. 1987; Elson & Walterbos 1988; Huchra, Brodie & Kent 1991; Barmby et al. 2000; Perrett et al. 2002; Fan et al. 2008; Galleti et al. 2009; Caldwell et al. 2009, 2011; Fan, de Grijs & Zhou 2010). Most of these studies have dealt with the regions comparatively close to the centre of M31, typically within 20–25 kpc in projection. This is because the relative proximity of M31 also poses a problem in that the full extent of its stellar halo subtends a substantial angle on the sky ($\gtrsim$20° in diameter) which is difficult to search uniformly for GCs, especially those with low luminosities and/or surface brightnesses. The Pan-Andromeda Archaeological Survey (PAndAS; McConnachie et al. 2009) almost completely obviates these issues: its imaging spans a very wide area, typically reaching a projected distance $R_{\rm proj} \sim 150$ kpc from M31[2] – and is yet sufficiently deep to allow the identification of even faint GCs.

With high-quality wide-field imaging such as that obtained for PAndAS, M31 halo GCs are much more easily located than those in more central regions where the background and crowding due to the M31 disc hinders reliable identification of star clusters in ground-based data. Halo GCs also offer the opportunity to study regions with very long dynamical time-scales that can preserve evidence of past events. If formed in situ, remote halo GCs will have been much less affected by tidal forces than those towards the centre; if accreted along with dwarf satellite galaxies, their properties may reflect the nature of the original hosts.

This paper continues and extends earlier investigations of the GC population of M31 by our group. In particular, it provides the final catalogue of halo GCs from PAndAS, greatly extending our previous surveys and results – specifically those of Huxor et al. (2008, hereafter Hux08) and Huxor et al. (2011, hereafter Hux11). In Hux08, we presented 40 new GCs from a precursor survey to PAndAS conducted using the Wide-Field Camera (WFC) on the Isaac Newton Telescope (INT) along with some early imaging from MegaCam on the Canada–France–Hawaii Telescope (CFHT), and updated the classifications of many entries in the Revised Bologna Catalogue (RBC)[3] – the most complete catalogue of M31 GCs, and widely used by the community.[4] Hux11 explored the 'ensemble' properties of the updated M31 GC sample from Hux08. In this paper, we exploit the full, final PAndAS data, searching for new GCs, investigating candidate GCs from the RBC, and updating many of the results from Hux11 with a particular focus on the properties of the GCs in the halo.

In addition to M31, the PAndAS data (and its preceding INT/WFC survey) also extend to M33, and our work on the GCs in this galaxy is published elsewhere (Huxor et al. 2009; Cockcroft et al. 2011). We have also used PAndAS imaging to discover new GCs in the M31 dwarf elliptical (dE) satellites NGC 147 and NGC 185 (three GCs and one GC, respectively), as described in Veljanoski et al. (2013b). Although, strictly speaking, these clusters reside within the halo of M31, we do not include them in this paper as they possess clearly identified (and intact) host galaxies.

The GCs listed in our previous catalogue (Hux08) provided targets for follow-up observations and analysis, both by our own group and by others. In particular, our *Hubble Space Telescope* (*HST*) observations of many of the halo GCs led to a number of studies of their colour–magnitude diagrams and structural properties (Mackey et al. 2007; Perina et al. 2009, 2011, 2012; Federici et al. 2012; Tanvir et al. 2012; Wang & Ma 2012). Many of those GCs were also observed spectroscopically with ground-based facilities – for example, Alves-Brito et al. (2009) observed several at high resolution with the Keck Telescope. Similarly, Ma (2012) used optical and 2MASS photometry of many of our GCs to estimate their ages, masses and metallicities.

This paper is the first of a series of works in which we use our catalogue to shed new light on the outer regions of the M31 halo. In an accompanying paper (Veljanoski et al. 2014), we investigate the kinematics of the remote GC system, while in two forthcoming works we will explore the relationship between the GCs and the underlying field halo, and the resolved properties of the GCs through *HST* imaging (Mackey et al. in preparation).

This paper proceeds as follows: in Section 2, we describe the CFHT/MegaCam data set we employed, and the strategy used to locate new GCs. The newly discovered GCs are then presented in Section 3. In addition to discovering new GCs, we also used the same imaging data to clean previous samples of published M31 GCs and GC candidates, and the results of this undertaking are given in Section 4. The photometry of our new clusters, and all other GCs with a galactocentric distance of greater than 25 kpc, is described and tabulated in Section 5. Next, we assess the completeness of our sample, critical to proper exploitation of the catalogue, in Section 6. Finally, in Section 7, we analyse the ensemble photometric properties of the M31 outer halo GC system, using our enlarged and improved catalogue.

2 THE GLOBULAR CLUSTER SURVEY

2.1 The data

The images and photometric catalogue employed in this study were taken from the now-completed PAndAS survey of M31, conducted using the CFHT on Mauna Kea, Hawaii. Details of this survey and its precursors can be found in a number of previous works (e.g. Martin et al. 2006; Ibata et al. 2007; McConnachie et al. 2008, 2009; Ibata et al. 2014), but we briefly summarize the key points here. The PAndAS imaging was undertaken with the MegaPrime/MegaCam camera mounted on the CFHT, which comprises 36 CCDs (each 2048 × 4612 pixels). Each pointing provides a usable field- of-view of 0.96 × 0.94 deg^2. Three dithered 450 s subexposures in each of the MegaCam g and i filters typically reach $g \approx 26.0$ and $i \approx 24.8$ (for point sources at the 5σ detection limit) once reduced and combined.

Crucial to our identification of GCs is the excellent PAndAS image quality. Many early exposures with relatively poor seeing were re-observed towards the end of the survey programme, resulting in a mean seeing of 0.67 arcsec in the g-band and 0.60 arcsec in the i-band, with an rms scatter between frames of 0.10 arcsec in both cases.

After initial reduction of the data at the CFHT, further image processing, calibration and photometric measurements were conducted at the Cambridge Astronomical Survey Unit (CASU). The CASU pipeline created final stacked g- and i-band images at each pointing, and a merged catalogue providing photometric data and star/galaxy classification for all detected sources, both stellar and non-stellar. The complete contiguous survey footprint, comprising 406 individual pointings, reaches to a projected distance of ∼150 kpc from M31 in most directions, thus encompassing almost the entire halo. This region is joined to a smaller area around M33, extending to ∼50 kpc from the centre of that galaxy.

[2] Although this is still some distance short of the likely virial radius of M31.
[3] http://www.bo.astro.it/M31/
[4] Note that at that time we worked with Version 3.0 of the RBC; for this work we refer to Version 5 from 2012 August.

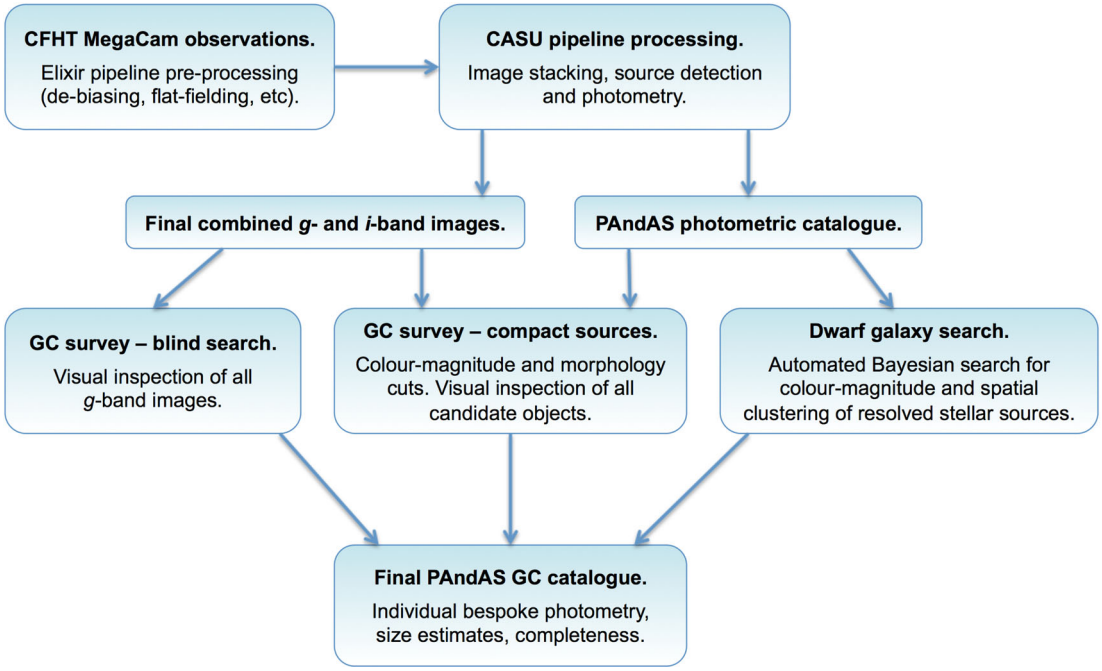

Figure 1. A schematic summary of our multistrand GC search strategy.

2.2 Search strategy

We adopted a multistrand search strategy based on our experience from Hux08, in which we found both classical 'compact' M31 GCs, and also the more diffuse 'extended' clusters. Our methodology is summarized in Fig. 1.

GC candidates were selected from the PAndAS photometric catalogue based on their magnitude and colour. Known GCs (both compact and extended) inhabit a broad range of absolute magnitudes and colours ($-10.5 < M_V < -3.5$, and $0.0 < (V-I)_0 < 1.7$) – limits which we converted to apparent MegaCam g and i-magnitudes by using the inverse of the transformation equations (1–4) described in Section 5, below, and assuming an M31 distance modulus of 24.47 and a typical foreground extinction $E(B-V) \sim 0.075$. We further required that any objects selected within these bounds have a non-stellar flag from the CASU photometric pipeline to be considered a GC candidate. This is appropriate for compact M31 GCs, which are always marginally resolved when the image quality is $\sim$0.6−0.7 arcsec. Diffuse clusters, however, tend not to appear in the catalogue as a single source and can therefore easily be missed with this approach – we adopted additional search techniques for these objects (see below). Note that the CASU pipeline is not optimized for non-stellar source photometry. Hence, although the magnitudes and colours are sufficiently accurate to identify likely compact GC candidates (especially given our very generous ranges for both), we subsequently undertook our own bespoke photometry of each GC we discovered (see Section 5).

We visually inspected a g-band image of every candidate object[5] and its local surrounding area, using a FITS image viewer to overlay (and so highlight) the positions of the GC candidates with graphic markers. This ensured that adequate attention was drawn to both the less luminous and the more compact candidates. At the distance of M31, and with the high quality of the MegaCam images, GCs generally take the form of a core that is slightly broader than the stellar point spread function (PSF), surrounded by resolved red giant branch stars. This results in an easily distinguished local 'halo' of such objects in well-populated clusters, and/or a broadened core with an irregular appearance for less luminous examples. In almost all cases, we found it straightforward to unambiguously classify a GC candidate as a cluster or not. However, the search efficiency was low – in the vast majority of instances the candidates turned out to be distant background galaxies.

Extended diffuse clusters (Huxor et al. 2005) are problematic because they are typically semi- or completely resolved across their full spatial extent in the MegaCam imaging and thus are not flagged in the PAndAS photometric catalogue by the presence of a single unresolved source. In most cases, however, such objects are also not sufficiently well populated or sufficiently uncrowded to appear as co-located groups of similar stars that could be detected by means of automated algorithms. Our previous experience (Hux08) showed that the most efficient and least biased way to detect such objects is by simple visual inspection of the full survey area. Although labour intensive, this inspection, conducted by APH, led to the discovery of many clusters ($\sim$30–40 per cent of our final sample) that would have otherwise been missed. In addition, it allowed us to independently confirm the nature of the compact clusters previously identified as described above, and ensure that no exceptional such objects lying outside the colour–magnitude selection box were missed. For quality control, to try and minimize the effects of human error, secondary inspection of roughly 30 per cent of the images was carried out separately by ADM. As a final measure, we looked for cluster detections in the automated search for M31 dwarf spheroidal galaxies conducted by NFM (Martin et al. 2013). These authors made use of both the spatial and colour–magnitude information of sources, in a probabilistic approach, to identify overdensities of stars with similar photometric properties. We quantitatively assess the completeness of our overall search strategy in Section 6.

[5] Our previous experience revealed that the g-band is both more effective and more efficient for identifying GCs than the i-band. This is largely due to the greatly reduced prominence of the main contaminants – background elliptical galaxies and foreground dwarf stars – in the blue.

2.3 Spatial coverage

Our search covered the PAndAS footprint to its largest radial extent, which ranges from ∼120–150 kpc in projection depending on the position angle relative to the M31 centre. However, the inner extent of our search is less clearly defined. The region which we examined uniformly includes the full area covered by the earlier INT/WFC survey as described in Hux08. As can be seen from fig. 4 of that paper, the inner region of the INT survey extended to an ellipse with a semimajor axis of 2° (∼27 kpc), and an inclination of 77°.5. Within this region variable crowding makes it difficult to conduct a uniform search for GCs, particularly affecting the discovery of low-luminosity compact GCs, and all extended GCs. Taking the above into account, we expect the completeness limits derived in Section 6 to be applicable outside a projected galactocentric radius of ∼25 kpc (although we did locate a handful of GCs within this radius).

3 THE NEWLY DISCOVERED CLUSTERS

Following the procedure described in Section 2, we discovered 58 previously unknown GCs and two additional GC candidates.[6] All but one of these came from the independent visual inspection of (i) candidates, and (ii) the full survey area. The exception, PAndAS-31, was discovered via the automated search for M31 dwarf spheroidal galaxies (see Martin et al. 2013). Note that, as described in that paper, the automated search also uncovered a small subset of the objects discovered independently in our search by eye.

The identity and location of each of these new objects are listed in Table 1, and *g*-band thumbnail images are shown in Fig. 2. The thumbnail images clearly reveal the unambiguous classification of each catalogued object as a GC, highlighting the quality of the data and the reason why our search turned up so few candidates with indeterminate classification. Of the two such candidates in our sample, Cand-01 is a faint object set against a relatively dense stellar background that hinders discrimination between its identity as a cluster or a distant galaxy, while Cand-02 is an extended object (cluster or distant galaxy) largely cut-off at the edge of an image. These are listed in Table 1 but not included in our subsequent analysis. We aim to obtain follow-up observations of these objects to clarify their status.

Note that with the 40 GCs presented in Hux08, we have found a total of ∼100 new GCs in the outer halo of M31.

For completeness, we note that a number of the clusters listed in Table 1 have formed the basis of previous studies – specifically those by Mackey et al. (2010b) and Veljanoski et al. (2013a) who investigated the ensemble properties of M31 halo GCs including subsamples from the present list, and the works by Mackey et al. (2013a,b) who studied specific objects (PA-48, and PA-7 and PA-8, respectively).

Our new catalogue represents the first detailed census of GCs across the full M31 halo, greatly extending the work of Hux08. The vast majority of our discoveries (53 of 59) lie in the outskirts of M31, at projected radii $R_{\rm proj} > 25$ kpc. Of these, a substantial fraction lie at distances that were completely unexplored prior to our CFHT campaign: our catalogue contains 21 clusters beyond $R_{\rm proj} = 80$ kpc, of which 11 sit outside $R_{\rm proj} = 100$ kpc. Indeed, we effectively find GCs out to distances commensurate with the edge of the PAndAS footprint, confirming previous suggestions that the

[6] We note that we subsequently also discovered one additional GC (PA-59), as detailed in Section 4.1.

Table 1. Locations of newly discovered PAndAS GCs.

ID	Position (J2000.0)		$R_{\rm proj}$
	RA	Dec.	(kpc)
PAndAS-01	23 57 12.03	+43 33 08.28	118.92
PAndAS-02	23 57 55.69	+41 46 49.25	114.74
PAndAS-03	00 03 56.41	+40 53 19.20	100.00
PAndAS-04	00 04 42.93	+47 21 42.47	124.62
PAndAS-05	00 05 24.15	+43 55 35.70	100.60
PAndAS-06	00 06 11.95	+41 41 20.97	93.66
PAndAS-07	00 10 51.35	+39 35 58.55	85.95
PAndAS-08	00 12 52.45	+38 17 47.86	88.26
PAndAS-09	00 12 54.66	+45 05 55.86	90.82
PAndAS-10	00 13 38.66	+45 11 11.13	90.00
PAndAS-11	00 14 55.63	+44 37 16.35	83.23
PAndAS-12	00 17 40.08	+43 18 39.02	69.21
PAndAS-13	00 17 42.72	+43 04 31.83	67.98
PAndAS-14	00 20 33.88	+36 39 34.46	86.20
PAndAS-15	00 22 44.07	+41 56 14.16	51.90
PAndAS-16	00 24 59.92	+39 42 13.11	50.81
PAndAS-17	00 26 52.20	+38 44 58.11	53.93
PAndAS-18	00 28 23.26	+39 55 04.86	41.55
PAndAS-19	00 30 12.22	+39 50 59.27	37.87
PAndAS-20	00 31 23.74	+41 59 20.12	30.59
PAndAS-21	00 31 27.52	+39 32 21.84	37.68
PAndAS-22	00 32 08.36	+40 37 31.62	28.73
PAndAS-23	00 33 14.13	+39 35 15.93	33.74
PAndAS-24	00 33 50.57	+38 38 28.04	42.81
PAndAS-25	00 34 06.15	+43 15 06.65	34.79
PAndAS-26	00 34 45.08	+38 26 38.05	43.92
PAndAS-27	00 35 13.53	+45 10 37.85	56.58
PAndAS-28	00 35 56.43	+40 48 44.98	18.60
PAndAS-29	00 36 09.08	+40 08 09.85	23.04
PAndAS-30	00 38 29.01	+37 58 39.21	46.35
PAndAS-31	00 39 59.79	+43 03 19.67	25.38
PAndAS-32	00 40 41.20	+40 00 54.95	17.94
PAndAS-33	00 40 57.35	+38 38 10.24	36.28
PAndAS-34	00 41 18.04	+42 46 16.51	20.85
PAndAS-35	00 43 09.36	+40 36 38.23	9.07
PAndAS-36	00 44 45.57	+43 26 34.79	30.14
PAndAS-37	00 48 26.53	+37 55 42.14	48.06
PAndAS-38	00 49 45.67	+47 54 33.12	92.33
PAndAS-39	00 50 36.22	+42 31 49.29	26.40
PAndAS-40	00 50 43.80	+40 03 30.20	26.51
PAndAS-41	00 53 39.58	+42 35 14.98	33.09
PAndAS-42	00 56 38.04	+39 40 25.93	42.18
PAndAS-43	00 56 38.80	+42 27 17.77	38.92
PAndAS-44	00 57 55.89	+41 42 57.01	39.35
PAndAS-45	00 58 37.96	+41 57 11.48	41.66
PAndAS-46	00 58 56.40	+42 27 38.29	44.31
PAndAS-47	00 59 04.78	+42 22 35.06	44.26
PAndAS-48	00 59 28.26	+31 29 10.64	141.34
PAndAS-49	01 00 50.07	+42 18 13.25	48.21
PAndAS-50	01 01 50.66	+48 18 19.22	106.68
PAndAS-51	01 02 06.61	+42 48 06.64	53.42
PAndAS-52	01 12 47.01	+42 25 24.87	78.05
PAndAS-53	01 17 58.41	+39 14 53.20	95.88
PAndAS-54	01 18 00.14	+39 16 59.93	95.79
PAndAS-55	01 19 20.41	+46 03 11.52	111.50
PAndAS-56	01 23 03.53	+41 55 11.02	103.34
PAndAS-57	01 27 47.51	+40 40 47.20	116.41
PAndAS-58	01 29 02.16	+40 47 08.66	119.42
PAndAS-59	00 36 29.53	+40 38 16.83	18.28
PAndAS-Cand-01	00 44 58.35	+40 21 37.92	13.70
PAndAS-Cand-02	01 07 53.88	+48 22 41.79	114.60

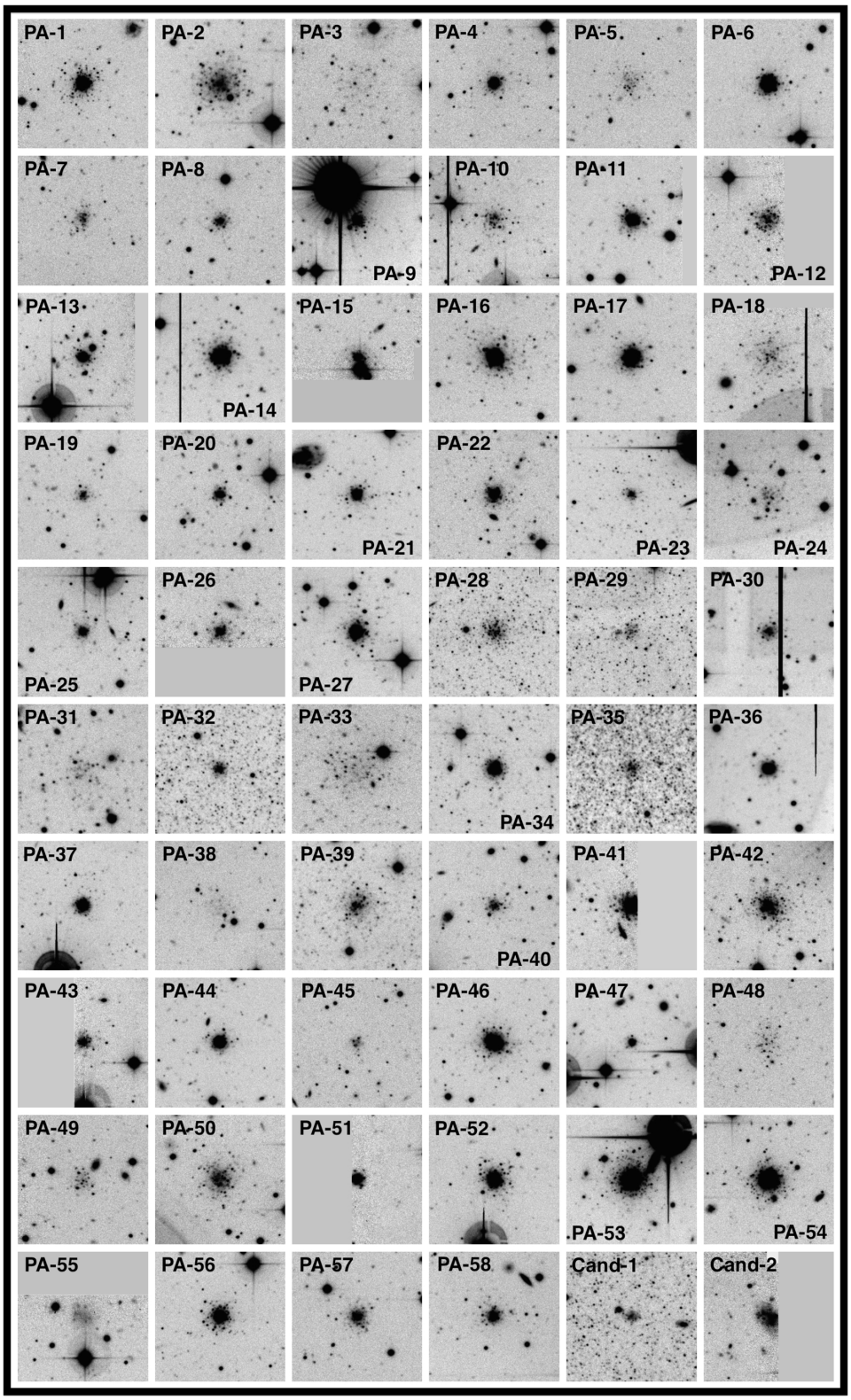

Figure 2. MegaCam *g*-band thumbnail images of our new M31 halo GCs. Each image is 1 arcmin × 1 arcmin in size, with north to the top and east to the left. PA-59 is shown in Fig. 4.

M31 cluster system is very extended (e.g. Mackey et al. 2010a) and suggesting that additional GCs may be found at even larger radii (see also di Tullio Zinn & Zinn 2013). Combined with previous discoveries, mostly from Hux08, we now know of 91 M31 GCs lying outside $R_{\rm proj} > 25$ kpc, which includes 12 at distances larger than $R_{\rm proj} = 100$ kpc.

These observations stand in stark contrast to the halo GC population in the MW, in which there are only ≈13 objects known at

Table 2. Updated GC classifications in the RBC V5.

Name in RBC V5	Position (J2000.0) RA	Dec.	R_{proj} (kpc)	Previous classification[a]	New classification[a]
Promoted GCs + H II					
PAndAS-59	00 36 29.35	+40 38 16.7	18.29	–	1
SH06	00 39 19.05	+40 21 58.0	15.19	2	5 (1?)
B270D	00 45 49.22	+41 01 49.3	8.57	2	1
SK213C	00 46 58.77	+42 17 45.3	17.71	2	1
SK255B	00 49 03.02	+41 54 57.8	18.39	2	1
Demoted GCs					
SK002A	00 36 34.99	+41 01 08.0	16.20	1	6
SK004A	00 38 01.35	+42 04 06.4	16.25	1	6
BA11	00 48 45.59	+42 23 37.7	21.71	1	4 + 6

[a]Classes: 1, 8 = GC; 2, 3 = candidate GC; 4 = galaxy; 5 = H II region; 6 = star.
[b]Classified as a candidate in previous versions of the RBC – see the text.

Galactocentric radii larger than 30−35 kpc (corresponding to an average projected radius of ∼25 kpc for random viewing angles), and in which the most distant known member sits at a Galactocentric distance of ≈120 kpc (corresponding to an average projected distance of ∼95 kpc for random viewing angles). While the disparity in the number of GCs in the MW and M31 within $R_{proj} \approx 25$ kpc is roughly 3:1 in favour of M31, our new catalogue reveals that outside this radius it is more like 7:1 in favour of M31. We explore the differences between these two GC systems in more detail in Section 7.

The photometric properties (luminosities, colours and sizes) of our new GC sample are derived below in Section 5. However, the excellent quality of PAndAS imaging also allowed us to examine and resolve the identity of many candidate clusters previously identified in the literature, and we first turn our attention to these.

4 UPDATES TO PUBLISHED CATALOGUES

There are two primary sources of candidate M31 halo clusters – the RBC (Galleti et al. 2004), and a recent search for M31 GCs in the Sloan Digital Sky Survey (SDSS) by di Tullio Zinn & Zinn (2013).

4.1 Revised Bologna Catalogue

The RBC is the main repository for information on the M31 GC system. It contains lists of confirmed GCs (classes 1 and 8 in the catalogue) and candidate GCs (classes 2 and 3), as well as a few H II regions (class 5), and compilations of objects once suspected to be GCs but subsequently revealed as background galaxies (class 4) or foreground stars (class 6). The identities of these contaminants are retained in the RBC in order to avoid misclassification in future GC surveys.

We inspected 1.5 arcmin × 1.5 arcmin PAndAS thumbnails of all objects listed in Version 5 of the RBC (released in 2012 August) as having projected galactocentric radii larger than $R_{proj} \sim 15$ kpc. Inside this radius the strong and variable background due to the M31 disc means that even with our high-quality PAndAS imaging it is frequently impossible to establish a reliable target classification.[7] Overall there are 523 objects with $R_{proj} \geq 15$ kpc in the RBC V5, of which 497 have PAndAS imaging. The missing 26 entries typically fall into small gaps in the coverage resulting from the inter-row CCD spaces on the MegaCam array (the spaces between individual CCDs on a given row were covered by the PAndAS dither pattern) or imperfect tiling of the PAndAS mosaic, although a couple sit outside the survey footprint with $R_{proj} \gtrsim 150$ kpc.

To avoid, as far as possible, prior knowledge introducing bias into our classifications, we employed a blind inspection methodology. One of us (ADM) generated thumbnails for all targets, randomized the order, and supplied the images only, with no supplementary information, to APH for classification. Once the inspection process was complete, the results were returned to ADM for analysis.

The original RBC classifications for the 497 objects we inspected broke down as follows: 72 GCs, 141 GC candidates, 166 background galaxies, 116 foreground stars and 2 H II regions. We confirmed that all 282 of the contaminant objects (galaxies and stars) were correctly identified as such. Of more interest are the GCs and GC candidates, and we were able to greatly improve classifications for these targets.

We found that two of the candidates were in fact genuine GCs. These objects are listed in Table 2 and their *g*-band thumbnails displayed in Fig. 3: SK213C and SK255B. Both are located within the 25 kpc inner limit of our main survey, which was why they were not identified as part of that search. We also uncovered one particularly interesting GC candidate – SH06, which consists of a compact luminous source surrounded by nebulosity that is quite evident in the *g*-band imaging (see Fig. 3) but virtually invisible in the *i* band. This is suggestive of a massive young star cluster still embedded in gas, sitting at ∼15 kpc from the M31 centre. However, because we cannot be absolutely certain that there is a cluster present, we conservatively classify this object as an H II region in Table 2.

While inspecting the object SK014B, which is correctly classified in the RBC V5 as a star, we noticed a small cluster nearby which does not appear anywhere in the RBC. We therefore believe this to be a new discovery, which we name PAndAS-59. We include PA-59 in Table 2 and display the discovery thumbnail in Fig. 4. That we identified this object serendipitously in our sample of small thumbnail images suggests that a full search of the inner M31 halo, between ∼15 and 25 kpc, may be quite fruitful – although we reiterate the caveat that the increased crowding would adversely affect the completeness of any such survey.

To our sample of new RBC GCs we also add B270D. At $R_{proj} = 8.57$ kpc, this object sits well inside both our inner PAndAS search radius, and our inner RBC inspection radius. In V5 of the RBC, it is classified as a candidate object; we uncovered its cluster status by chance. It is listed in Table 2 and displayed in Fig. 3.

[7] Note that this radius is smaller than the inner radius of our uniform survey ($R_{proj} = 25$ kpc) as here we are not trying to discover new GCs, but rather establish classifications for objects for which we already have positions.

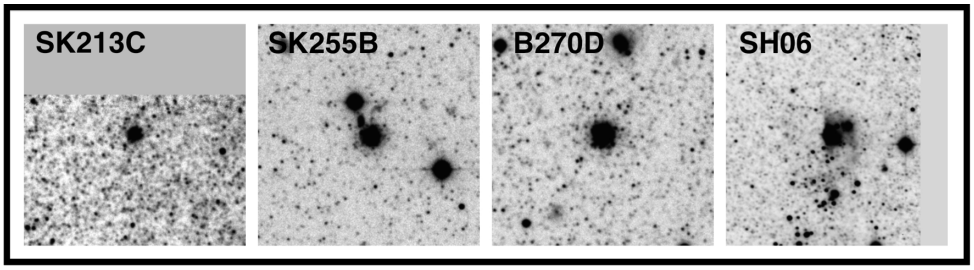

Figure 3. PAndAS *g*-band thumbnails for the three new GCs uncovered in the RBC V5, plus SH06 (see the text). Each thumbnail is 1 arcmin × 1 arcmin in size, with north to the top and east to the left.

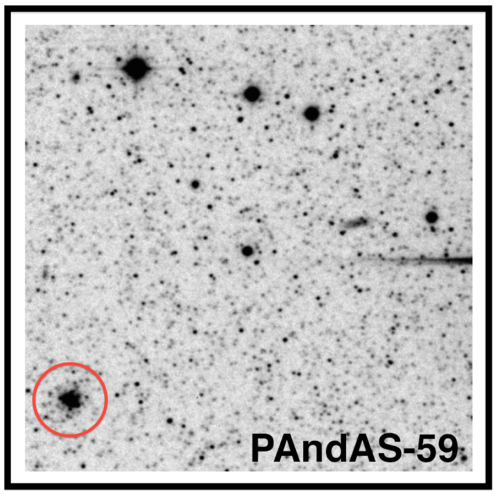

Figure 4. PAndAS *g*-band thumbnail for our serendipitous discovery PAndAS-59 (circled). The object at the centre of the field is SK014B, correctly classified in the RBC as a star. The thumbnail is 1.5 arcmin × 1.5 arcmin, with north to the top and east to the left.

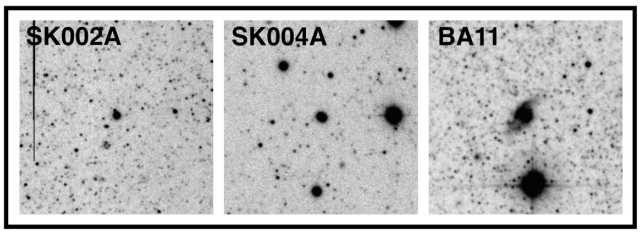

Figure 5. PAndAS *g*-band thumbnails for objects mis-classified as GCs in the RBC V5. Each thumbnail is 1 arcmin × 1 arcmin in size, with north to the top and east to the left. SK002A is a star; SK004A is two barely-separated stars; and BA11 is a star superimposed on a background galaxy.

In addition to confirming several new GCs among RBC candidates, we also found three 'confirmed' RBC GCs which were misclassified stars or galaxies. These objects – SK002A, SK004A, and BA11 – are listed in Table 2 and their thumbnails shown in Fig. 5.

All but one of the remaining 138 objects originally listed as GC candidates in the RBC V5 are either foreground stars (25 objects) or background galaxies (112 objects). These are listed in Table 3, and a few representative examples are displayed in Fig. 6. For the last candidate, BH01, we could not find any object at the listed coordinates. This is likely because BH01 is a very faint object identified from *HST* WFPC2 imaging (Barmby & Huchra 2001). The thumbnail for this target is also displayed in Fig. 6.

Finally, of the two H II regions listed in our sample, we found no compelling reason to alter the classification of one (DAO88), while at the coordinates of the second, B488, we found a dispersed sample of luminous blue stars and a small amount of nebulosity. This is consistent with its classification as an H II region; however, we note that there may possibly also be a young cluster at this location. A thumbnail for this object is shown in Fig. 6.

In summary, we inspected PAndAS thumbnails for 497 objects listed at $R_{\rm proj} \geq 15$ kpc in the RBC V5. Of these, 141 were originally classified as GC candidates; we were able to reclassify these as genuine GCs (2 objects) plus an H II region with a possible embedded young massive cluster, foreground stars (25 objects), and background galaxies (112 objects), while in one case no object was visible. Of the 72 targets originally listed as definite GCs, we confirmed 69 but found that three were either foreground stars or background galaxies. We did not change the classification of the two H II regions in the RBC list, and we confirmed the identity of the 282 objects originally listed as contaminants. Finally, we added two more new GCs (B270D and PAndAS-59) located by chance as discussed above.

4.2 Candidates from SDSS

During the preparation of this paper, di Tullio Zinn & Zinn (2013, hereafter dTZZ13) released a catalogue of M31 GCs and GC candidates derived from SDSS imaging. The area covered by SDSS overlaps substantially with the PAndAS footprint, allowing us to check the identity of many of the objects in the dTZZ13 catalogue – although a number also lie well beyond the edge of the PAndAS coverage.

The dTZZ13 catalogue consists of two primary lists. The first contains 18 objects classified as high-confidence GCs, while the second contains 75 lower confidence candidate GCs. We located 17 of the high-confidence targets in our PAndAS imaging, along with 42 of the candidates, and assessed these in the same manner as for objects in the RBC. The remaining dTZZ13 targets are at large radii from M31, $150 \lesssim R_{\rm proj} \lesssim 230$ kpc, and thus do not lie within the PAndAS footprint.

We found that 10 of the 17 high-confidence objects that we inspected are indeed GCs, the remaining 7 being either stars or distant galaxies. Classifications for these objects are listed in Table 4. All but three of the 10 GCs appear independently in our PAndAS catalogue, as indicated in the table. The three outstanding clusters are at relatively small projected radii, $R_{\rm proj} \lesssim 20$ kpc, and thus fall within the inner limiting radius of our uniform search area. This adds further weight to the suggestion from our RBC work above that a thorough search for GCs in the inner M31 halo may be fruitful. We show *g*-band thumbnails of the three new SDSS clusters in Fig. 7.

Table 3. Updated classifications for GC candidates listed in the RBC V5.

Name in RBC V5	Position (J2000.0) RA	Dec.	R_{proj} (kpc)	New class[a]	Name in RBC V5	Position (J2000.0) RA	Dec.	R_{proj} (kpc)	New class[a]
SK001C	00 33 13.080	+40 05 26.00	29.47	4	SK019B	00 37 33.470	+40 05 28.70	20.96	4
SK002C	00 33 15.820	+40 00 24.70	30.03	4	SK020B	00 37 35.680	+40 35 14.40	16.22	4
SK001B	00 33 23.070	+40 04 40.70	29.21	4	SK048C	00 37 37.200	+40 05 39.60	20.83	4
SK002B	00 33 32.200	+39 51 32.80	30.70	4	SK049C	00 37 37.270	+41 54 04.40	15.67	4
SK004C	00 33 34.960	+40 08 16.30	28.32	4	SK050C	00 37 41.270	+40 04 42.90	20.89	4
SK003B	00 33 37.030	+39 40 59.00	32.14	4	SK051C	00 37 41.790	+40 05 18.00	20.77	4
SK005C	00 33 38.040	+39 35 35.70	32.96	4	SK022B	00 37 54.310	+40 17 26.70	18.31	4
SK006C	00 33 46.110	+39 48 36.60	30.67	4	SK053C	00 38 00.760	+42 02 56.90	16.10	4
SK007C	00 33 54.630	+39 34 36.60	32.61	4	SK054C	00 38 06.100	+40 24 30.20	16.80	6
B133D	00 34 10.994	+39 50 50.27	29.52	4	SK058C	00 38 48.400	+40 03 01.20	19.53	4
BH01[b]	00 34 11.480	+39 23 59.10	33.90	–	SK066C	00 39 15.190	+42 22 50.70	17.59	6
SK009C	00 34 12.200	+40 06 29.70	27.22	4	B186D	00 40 02.258	+39 23 12.11	26.68	4
SK010C	00 34 26.850	+39 54 05.60	28.51	4	SK073C	00 40 04.300	+40 14 10.70	15.72	4
B411	00 34 30.808	+41 33 44.09	21.46	4	B188D	00 40 14.038	+39 41 30.82	22.52	4
SK004B	00 34 34.200	+40 02 49.40	26.98	4	B191D	00 40 17.893	+42 25 23.98	16.95	4
SK011C	00 34 51.160	+39 55 33.10	27.50	4	SK090C	00 40 53.060	+40 00 43.30	17.84	4
B412	00 34 55.281	+41 32 26.49	20.38	4	B460	00 41 54.817	+39 35 25.51	23.05	4
SK012C	00 35 08.810	+40 07 32.60	25.13	4	SK104C	00 42 03.040	+40 03 48.80	16.58	4
SK013C	00 35 09.240	+40 05 39.80	25.38	4	SK110C	00 42 33.090	+40 04 53.60	16.24	4
B413	00 35 13.001	+41 29 07.81	19.51	4	B225D	00 43 13.440	+40 01 14.58	17.11	6
BA22	00 35 13.608	+39 45 37.16	28.40	4	B233D	00 43 41.311	+39 36 45.96	22.78	4
SK014C	00 35 14.860	+39 41 40.00	29.03	4	SK136C	00 44 04.430	+40 05 19.60	16.50	6
SK015C	00 35 20.470	+39 35 04.10	30.02	4	SK160C	00 44 54.430	+40 06 44.10	16.78	4
SK016C	00 35 22.000	+41 49 47.40	20.35	4	SK205B	00 45 33.250	+40 17 08.40	15.29	4
SK017C	00 35 28.440	+39 32 25.10	30.27	6	SK193C	00 45 49.970	+40 05 09.10	18.05	4
SK018C	00 35 29.320	+41 42 33.30	19.51	4	SK196C	00 45 51.580	+40 04 43.80	18.17	4
B134D	00 35 30.298	+40 44 24.84	20.01	4	SK214B	00 45 54.060	+39 56 46.80	19.86	6
SK006B	00 35 34.240	+41 11 53.00	18.45	4	SK197C	00 45 57.630	+40 17 09.50	15.82	4
SK007B	00 35 45.260	+39 39 21.30	28.57	4	SK200C	00 46 06.090	+40 22 26.00	15.01	4
SK020C	00 35 49.740	+41 50 02.40	19.28	4	SK221B	00 46 19.240	+40 23 42.00	15.12	6
SK021C	00 35 50.830	+39 36 00.80	29.02	4	B281D	00 46 22.279	+40 18 08.00	16.22	6
SK022C	00 35 51.760	+40 54 11.60	18.40	4	SK204C	00 46 22.920	+40 20 42.20	15.76	4
SK023C	00 35 53.100	+41 51 23.70	19.27	4	SK223B	00 46 32.880	+40 06 36.50	18.67	6
SK024C	00 35 53.830	+41 43 42.60	18.60	4	B488[c]	00 46 34.287	+42 11 42.78	15.99	5
SK025C	00 35 54.220	+41 46 53.80	18.84	4	B489	00 46 36.386	+40 00 26.86	19.95	4
SK008B	00 35 58.150	+39 37 35.50	28.54	4	SH21	00 46 37.308	+39 23 57.85	27.49	6
SK009B	00 36 00.230	+40 56 19.20	17.92	4	B291D	00 46 41.270	+40 03 02.00	19.55	6
SK010B	00 36 01.700	+39 48 50.20	26.45	4	B293D	00 46 48.097	+40 02 21.72	19.84	6
SK011B	00 36 02.020	+41 14 43.40	17.23	4	B390	00 46 51.632	+40 23 46.90	16.00	6
SK026C	00 36 05.610	+39 58 04.90	24.77	4	SK231B	00 47 14.110	+40 22 23.20	16.89	6
SK029C	00 36 22.260	+39 52 04.50	25.30	4	BA28	00 47 14.220	+42 21 42.20	18.82	4
B139D	00 36 24.679	+39 45 07.43	26.47	6	SK232B	00 47 14.430	+40 25 38.80	16.36	4
SK030C	00 36 27.360	+41 35 14.00	16.67	4	DAO93	00 47 46.178	+42 44 55.88	23.92	4
SK031C	00 36 31.430	+42 06 24.60	19.56	4	DAO94	00 47 54.399	+42 44 01.58	23.94	4
SK013B	00 36 31.700	+41 11 41.30	15.99	4	BA10	00 47 56.286	+42 28 43.73	21.18	4
SK032C	00 36 33.360	+41 30 03.10	16.16	4	SK222C	00 47 59.480	+41 54 13.00	15.98	6
B142D	00 36 33.831	+41 09 07.96	15.95	4	SK238B	00 48 01.660	+41 49 56.90	15.56	6
B144D	00 36 36.647	+41 37 03.65	16.40	6	SK223C	00 48 04.610	+40 08 27.00	20.72	4
SK033C	00 36 37.890	+42 14 46.20	20.51	4	SH24	00 48 15.545	+42 25 17.12	21.11	6
SK034C	00 36 43.420	+39 34 56.20	27.87	4	SK240B	00 48 24.140	+40 06 43.10	21.58	4
SK035C	00 36 46.660	+41 26 23.90	15.47	4	SK243B	00 48 27.190	+42 02 43.50	18.04	4
SK036C	00 36 47.200	+40 04 09.50	22.52	4	SK225C	00 48 31.340	+42 01 05.50	17.97	4
SK037C	00 36 49.190	+39 39 43.70	26.82	4	SK249B	00 48 32.960	+42 02 45.00	18.24	4
SK039C	00 37 00.980	+39 33 27.60	27.74	6	SK252B	00 48 41.130	+41 31 54.60	15.66	6
SK040C	00 37 03.400	+41 33 22.10	15.08	6	SK227C	00 48 44.050	+42 15 48.80	20.45	4
SK041C	00 37 05.080	+40 01 06.30	22.52	4	B504	00 48 45.168	+40 08 45.94	21.87	4
SK042C	00 37 06.280	+41 44 48.50	15.82	4	SK228C	00 48 46.490	+41 46 45.80	16.94	4
SK043C	00 37 09.100	+39 49 10.40	24.56	6	DAO99	00 48 48.314	+42 32 45.20	23.29	4
SK046C	00 37 28.930	+41 55 01.90	16.09	4	B334D	00 48 54.848	+39 35 56.07	27.92	4
SK017B	00 37 30.440	+40 36 43.80	16.22	4	SK256B	00 49 05.380	+41 57 38.30	18.78	4
SK018B	00 37 30.820	+40 18 23.90	18.86	4	SK229C	00 49 11.040	+41 57 53.10	19.01	4

Table 3 – *continued*

Name in RBC V5	Position (J2000.0) RA	Dec.	R_{proj} (kpc)	New class[a]	Name in RBC V5	Position (J2000.0) RA	Dec.	R_{proj} (kpc)	New class[a]
SK257B	00 49 15.210	+41 01 29.40	17.09	6	B346D	00 50 03.750	+40 37 39.28	20.84	4
B338D	00 49 15.765	+40 46 23.47	18.14	4	SK258B	00 50 17.460	+42 06 42.60	22.45	4
B339D	00 49 17.493	+40 45 06.58	18.32	4	B348D	00 50 19.219	+40 58 02.78	19.95	4
DAO104	00 49 21.347	+42 16 16.60	21.73	4	B511	00 50 43.418	+40 11 13.39	25.43	4
SK232C	00 49 25.630	+42 06 06.70	20.52	4	B512	00 50 46.324	+39 53 19.91	28.13	4
B340D	00 49 29.174	+41 04 32.10	17.56	4	B513	00 50 47.806	+41 25 46.27	20.79	4
B506	00 49 34.905	+40 00 28.94	24.74	4	G355	00 51 33.740	+39 57 35.81	29.06	4
SK233C	00 49 35.650	+42 11 42.80	21.58	4	SH25	00 52 04.054	+41 35 05.85	24.29	4
B345D[d]	00 49 52.554	+40 53 10.10	19.12	6					

[a]All objects were originally classified as cluster candidates (class 2 or 3) except for B488 (class 5).
[b]No object is visible at the coordinates specified for BH01. This is a very faint candidate from archival *HST* imaging.
[c]We retain the classification of B488 as an H II region but note there may also be a young cluster at this location.
[d]B345D appears to be a star superposed on a galaxy, so could also be classed as 4.

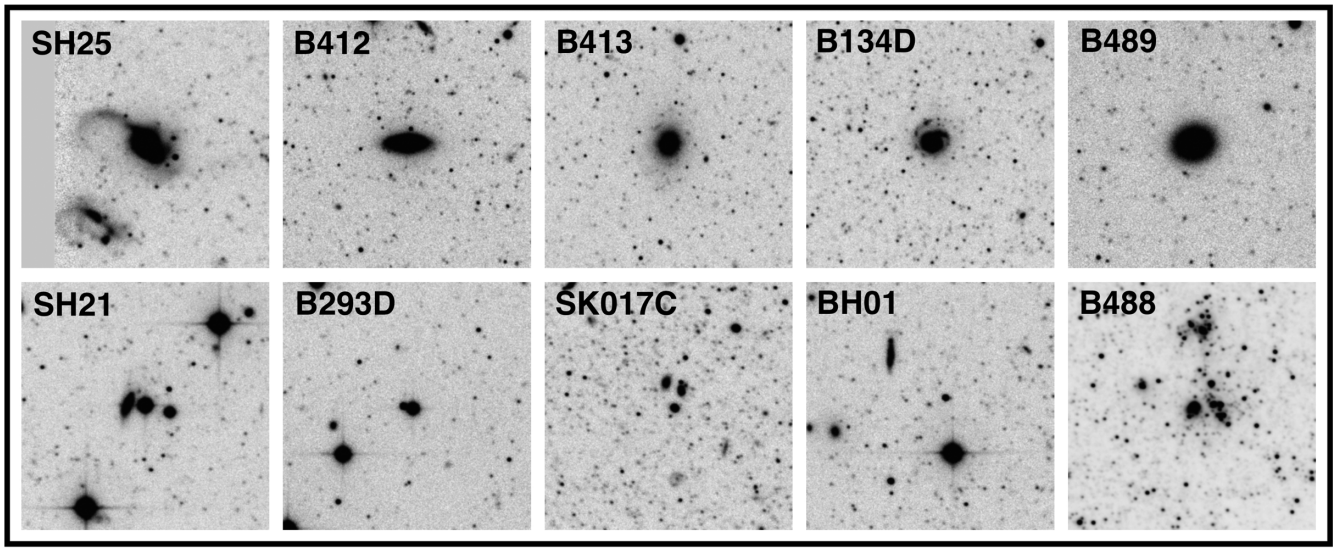

Figure 6. PAndAS *g*-band thumbnails for representative examples of objects classified as GC candidates in the RBC V5, that are galaxies (upper row) or stars (lower row, left three panels). In addition we include on the lower row images for BH01, for which no object is visible at the listed coordinates, and B488, which is a H II region that may also contain a dispersed young cluster. Each thumbnail is 1 arcmin × 1 arcmin in size, with north to the top and east to the left.

Table 4. Confirmed GCs in the dTZZ13 catalogue.

Name in dTZZ13	PAndAS name	Position (J2000.0) RA	Dec.	R_{proj} (kpc)
SDSS1	–	00 36 01.8	+40 29 50	20.29
SDSS3	–	00 39 13.1	+41 42 08	10.78
SDSS4	PA-34	00 41 18.0	+42 46 16	20.84
SDSS6	–	00 42 27.6	+39 55 28	18.39
SDSS8	PA-39	00 50 36.3	+42 31 50	26.40
SDSS9	PA-41	00 53 39.6	+42 35 15	33.09
SDSS11	PA-46	00 58 56.4	+42 27 38	44.31
SDSS12	PA-52	01 12 47.0	+42 25 25	78.05
SDSS15	PA-56	01 23 03.5	+41 55 11	103.34
SDSS16	PA-58	01 29 02.2	+40 47 09	119.42
C62	PA-57	01 27 47.6	+40 40 48	116.41

Of the 42 candidate objects inspected, we only confirmed 1 as a genuine GC. This is C62, which we also list in Table 4 and which also appears in our PAndAS catalogue. All of the other candidate objects turned out to be background galaxies; we list these in Table 5.

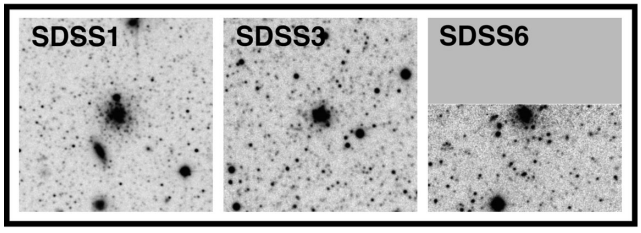

Figure 7. PAndAS *g*-band thumbnails for the three confirmed non-PAndAS GCs in the SDSS catalogue of di Tullio Zinn & Zinn (2013). Each thumbnail is 1 arcmin × 1 arcmin in size, with north to the top and east to the left.

Based on a simple extrapolation of our results, it is moderately likely (∼60 per cent) that the remaining high-confidence object from dTZZ13 – SDSS17, which falls at $R_{proj} \sim 158$ kpc – is a GC. However, the success rate from their lower confidence candidate list is substantially smaller (∼2.4 per cent), suggesting that in the group of 33 such objects that we were unable to inspect there may be at most one or two genuine GCs. Nonetheless, with $R_{proj} > 150$ kpc, it would be very worthwhile tracking these down.

Table 5. Non-clusters in the dTZZ13 catalogue.

Name in dTZZ13	Position (J2000.0) RA	Dec.	R_{proj} (kpc)	Class
SDSS2	00 38 26.9	+40 12 35	18.25	4
SDSS5	00 41 47.2	+41 44 10	6.83	4
SDSS7	00 47 41.1	+42 04 17	16.72	4
SDSS10	00 55 28.1	+43 59 31	49.06	4
SDSS13	01 16 41.7	+33 19 25	142.35	4
SDSS14	01 22 20.7	+35 11 35	134.73	4
SDSS18	23 49 09.7	+40 27 30	138.73	4
C2	00 08 19.0	+34 28 07	131.23	4
C3	00 08 34.5	+34 37 38	129.14	4
C14	00 39 32.3	+40 51 17	10.00	4
C15	00 40 09.5	+39 55 30	19.55	4
C16	00 40 14.0	+39 02 33	31.13	4
C17	00 40 31.9	+38 11 12	42.52	4
C18	00 41 38.9	+37 19 34	53.96	4
C20	00 42 09.2	+38 56 15	31.90	4
C22	00 43 03.7	+32 08 37	124.71	4
C23	00 43 32.0	+33 10 04	110.73	4
C24	00 43 44.3	+31 41 24	130.93	4
C26	00 44 01.0	+30 42 01	144.48	4
C27	00 45 40.2	+37 47 11	48.22	4
C30	00 48 25.4	+29 16 03	164.77	4
C31	00 49 33.1	+34 52 00	89.39	4
C32	00 49 37.5	+33 44 54	104.45	4
C33	00 50 22.5	+41 51 35	21.12	4
C34	00 51 12.0	+43 33 35	37.88	4
C36	00 51 32.6	+41 57 24	24.37	4
C37	00 51 47.3	+41 37 32	23.68	4
C39	00 52 34.6	+43 18 25	37.33	4
C40	00 54 06.3	+29 55 18	158.23	4
C41	01 00 12.7	+34 00 43	109.83	4
C45	01 05 43.0	+30 56 43	154.59	4
C47	01 06 14.8	+34 01 15	117.64	4
C48	01 06 40.5	+32 29 59	136.44	4
C50	01 08 33.5	+33 47 10	123.81	4
C51	01 09 40.6	+34 14 13	120.46	4
C52	01 10 50.8	+44 44 38	84.72	4
C55	01 14 29.6	+46 06 07	102.46	4
C56	01 17 36.0	+46 11 18	109.10	4
C58	01 19 43.8	+33 09 20	149.57	4
C59	01 22 56.7	+42 14 39	103.27	4
C60	01 26 10.8	+43 49 11	114.66	4
C61	01 27 37.6	+38 07 05	125.50	4
C63	01 28 38.6	+44 00 47	121.18	4
C65	01 31 17.4	+45 43 43	134.68	4
C66	01 32 45.8	+42 57 32	128.74	4
C67	01 33 59.1	+42 38 02	131.41	4
C68	01 34 06.0	+45 43 32	140.88	4
C69	01 34 39.5	+44 05 41	135.82	4

5 CLUSTER PHOTOMETRY AND SIZES

5.1 Integrated luminosities

We performed aperture photometry on each of our 59 newly discovered GCs using the *phot* task in IRAF. We also photometered our two GC candidates, the additional six newly confirmed GCs from the RBC and dTZZ13 listed in Tables 2 and 4, SH06, and, to ensure a complete uniform sample of measurements for the outer M31 system, all other known GCs lying at $R_{proj} \geq 25$ kpc (38 objects, predominantly from Hux08). Our results may be found in Table 6.

For each target, we used *phot* to measure the flux in concentric apertures of increasing radius, and constructed a curve-of-growth. We employed the centroiding algorithm in the *phot* task to accurately determine the cluster centres.[8] This worked very well except on the most diffuse objects in our sample, which are fully resolved in the PAndAS imaging. For such targets, we determined the centroid by eye, and verified that our photometric measurements were robust to changes of a few pixels ($\sim$0.5 arcsec) in any direction about this point. For each GC, we combined the central coordinates determined (independently) from the *g*- and *i*-band images in a straight average, and these are the positions reported in Table 1. In all cases the difference in coordinates from the *g*- and *i*-band images was less than 0.3 arcsec, and in most cases less than 0.1 arcsec. To estimate the background flux for a given GC we used the median level in an annulus of width 10 arcsec sitting outside the selected maximum photometry aperture. In practice, the precise position of this background annulus was necessarily determined iteratively together with the maximum aperture itself.

For an isolated cluster with little or no foreground or background contamination, we would define the maximum aperture r_{max} to sit at a point where the increase in cumulative flux with radius (i.e. the curve-of-growth) is flat – thus ensuring the inclusion of essentially all cluster light in the measurement. Fig. 8 shows an example for the GC PA-27. However, only $\sim$60 per cent of our systems conform to this ideal. A few objects are badly impacted by their proximity to the edge of a CCD (e.g. B517), a very bright star (H13, PA-9) or galaxy (HEC11), or, for more centrally located clusters ($R_{proj} < 25$ kpc), the presence of moderately dense M31 field populations (e.g. PA-32, PA-35). Such cases cannot easily be corrected and thus for this type of object we were forced to artificially constrain r_{max} to a point on the curve-of-growth where the gradient is not necessarily flat, leading to an underestimate in the flux. Note that wherever possible in this situation we kept the background annulus substantially outside the enforced limiting radius for photometry so as to avoid any cluster contribution to the estimated background level – although in such cases this would never be the dominant source of uncertainty in any event. On a few rare occasions (e.g. PA-51, PA-55), a cluster fell so close to a CCD edge that it was only (partially) visible in one passband. In this situation, useful photometry is not possible.

The most common non-ideal scenario we encountered fell between the two extremes of a completely isolated cluster and an object severely impacted by a chip edge or an excessively bright local contaminant. Typically, a given target might have an unrestricted maximum aperture, but a few ($\lesssim$5) sources lying within this aperture that were obviously either background galaxies or foreground stars of sufficient brightness to noticeably impact the measured flux. In general, we found it straightforward to mask these objects such that the affected pixels were not used in the flux calculation. We also note that a few clusters (e.g. G1, PA-53) are sufficiently bright so as to be mildly saturated at their centres in the PAndAS imaging. While this affects the shape of the curve-of-growth at small radii, in no case was the saturation severe enough to alter the total flux measured within r_{max}.

Given the variety of different circumstances seen across our sample, we assigned a flag to each object to indicate the quality of the photometric measurement. These sit on a scale of A–D, with the following meanings:

[8] Note that our calculated coordinates for PA-31, and the handful of other GCs detected by Martin et al. (2013), are somewhat different than those listed in that paper. This is because Martin et al. report the coordinates of the spatial grid point in their calculation corresponding to the local probability maximum. The coordinates determined here are more accurate.

Table 6. Photometric measurements for PAndAS GCs and selected others.

Cluster name	$E(B-V)$	r_{max} (arcsec)	g	i	$(g-i)_0$	M_V	$(V-I)_0$	r_h (pc)	Quality Flag	Notes
PAndAS-1	0.099	14.8	17.55	16.74	0.62	−7.48	0.83	7.1	A	–
PAndAS-2	0.106	19.2	18.30	17.29	0.70	−6.82	0.90	25.7	A	–
PAndAS-3	0.087	13.9	20.89	19.90	0.65	−4.17	0.86	27.4	B	c
PAndAS-4	0.133	14.1	18.07	17.17	0.69	−7.09	0.89	4.7	A	–
PAndAS-5	0.078	11.8	19.94	19.08	0.79	−5.05	0.97	17.0	A	c
PAndAS-6	0.068	14.1	16.92	16.15	0.67	−8.02	0.87	4.4	A	–
PAndAS-7	0.088	11.8	20.18	18.77	0.70	−5.00	0.89	13.3	A	c
PAndAS-8	0.109	10.4	19.89	18.29	0.87	−5.40	1.03	9.5	A	–
PAndAS-9	0.090	5.2	18.23	17.51	0.62	−6.75	0.83	3.8	C	b,r*
PAndAS-10	0.094	12.2	19.61	18.75	0.75	−5.43	0.93	15.2	A	c
PAndAS-11	0.088	12.6	18.29	17.41	0.67	−6.74	0.87	9.4	A	–
PAndAS-12	0.060	7.4	19.63	18.72	0.75	−5.33	0.94	13.7	B	e,r
PAndAS-13	0.063	7.4	18.43	17.66	0.65	−6.49	0.85	4.7	B	m,b,r
PAndAS-14	0.069	12.6	17.93	17.17	0.71	−7.01	0.90	10.9	A	–
PAndAS-15	0.069	3.7	19.92	19.08	0.74	−5.04	0.93	6.0	C	b,e,r*
PAndAS-16	0.072	16.3	16.54	15.66	0.79	−8.44	0.97	5.5	A	–
PAndAS-17	0.067	14.1	16.87	15.77	1.00	−8.17	1.14	4.4	A	–
PAndAS-18	0.062	14.8	19.61	18.71	0.76	−5.35	0.94	23.0	A	c
PAndAS-19	0.055	8.1	20.17	19.39	0.72	−4.73	0.91	7.3	A	–
PAndAS-20	0.067	8.1	19.57	18.58	0.83	−5.43	1.00	7.4	A	–
PAndAS-21	0.054	14.1	17.84	17.06	0.67	−7.06	0.87	4.0	A	–
PAndAS-22	0.063	10.4	18.79	17.87	0.91	−6.18	1.06	7.3	A	–
PAndAS-23	0.054	6.7	19.98	18.89	1.04	−5.02	1.17	6.7	A	–
PAndAS-24	0.059	11.8	20.27	19.39	0.73	−4.68	0.91	16.9	A	c
PAndAS-25	0.064	4.8	19.78	18.80	0.88	−5.21	1.04	6.6	B	b,r
PAndAS-26	0.061	5.6	19.88	18.92	0.94	−5.10	1.09	7.4	B	e,r
PAndAS-27	0.075	14.8	17.31	16.41	0.75	−7.69	0.93	5.2	A	–
PAndAS-28	0.066	8.3	19.26	18.56	0.64	−5.65	0.85	12.7	B	f,r
PAndAS-29	0.058	5.2	20.58	19.75	0.72	−4.35	0.91	10.7	B	c,f,r
PAndAS-30	0.064	7.4	19.57	18.58	0.79	−5.42	0.96	10.9	A	c
PAndAS-31	0.073	9.3	20.62	19.60	0.82	−4.41	0.99	18.5	B	c,m
PAndAS-32	0.075	6.7	19.48	18.37	0.97	−5.58	1.11	8.0	B	f,r
PAndAS-33	0.059	18.5	19.56	18.67	0.68	−5.39	0.88	35.8	B	c,b
PAndAS-34	0.068	12.6	18.37	17.38	0.81	−6.64	0.98	10.4	A	–
PAndAS-35	0.086	5.2	19.91	18.59	1.09	−5.24	1.21	10.3	B	c,f,r
PAndAS-36	0.073	10.4	17.69	16.79	0.75	−7.30	0.94	5.8	A	–
PAndAS-37	0.057	9.6	17.66	16.56	1.00	−7.35	1.13	4.6	A	–
PAndAS-38	0.159	13.9	20.76	19.75	0.61	−4.50	0.83	24.4	B	c,m
PAndAS-39	0.086	9.6	18.85	17.90	0.88	−6.19	1.04	13.0	B	c,f,r
PAndAS-40	0.058	10.0	19.80	18.97	0.77	−5.13	0.95	10.0	A	–
PAndAS-41	0.096	–	–	–	–	–	–	–	D	e,r*
PAndAS-42	0.060	15.5	18.54	17.04	0.89	−6.59	1.05	15.4	C	c,b
PAndAS-43	0.093	4.4	19.79	18.85	0.79	−5.27	0.97	6.0	B	c,e,r
PAndAS-44	0.062	9.6	17.18	16.48	0.61	−7.72	0.82	3.1	A	–
PAndAS-45	0.083	7.4	20.97	20.05	0.79	−4.06	0.96	8.9	B	c
PAndAS-46	0.072	16.3	16.27	15.52	0.64	−8.67	0.85	4.3	B	s
PAndAS-47	0.070	5.6	19.39	18.26	1.01	−5.66	1.14	3.8	A	–
PAndAS-48	0.066	13.7	20.21	19.41	0.59	−4.73	0.81	21.2	A	c
PAndAS-49	0.067	11.1	20.24	19.11	0.92	−4.81	1.07	16.4	A	–
PAndAS-50	0.163	14.8	18.93	17.78	0.95	−6.38	1.10	17.1	A	–
PAndAS-51	0.074	–	–	–	–	–	–	–	D	e,x
PAndAS-52	0.063	13.3	17.38	16.49	0.78	−7.58	0.96	6.5	B	b
PAndAS-53	0.053	12.6	15.79	15.07	0.64	−9.09	0.85	4.2	B	s,b,r
PAndAS-54	0.053	12.6	16.30	15.57	0.63	−8.58	0.84	5.1	C	b,m
PAndAS-55	0.070	–	–	–	–	–	–	–	D	e,x
PAndAS-56	0.050	14.1	17.27	16.45	0.70	−7.63	0.89	4.7	A	–
PAndAS-57	0.066	8.9	19.24	18.44	0.71	−5.70	0.91	10.3	A	c
PAndAS-58	0.062	11.5	18.82	17.83	0.88	−6.17	1.04	9.3	A	–
PAndAS-59	0.068	3.7	19.96	19.32	0.53	−4.93	0.76	5.6	B	f,r
PAndAS-Ca1	0.067	4.4	20.84	20.27	0.45	−4.03	0.70	8.1	B	f,r
PAndAS-Ca2	0.175	4.4	20.02	19.08	0.65	−5.26	0.86	10.4	C	e,r*

Table 6. *– continued*

Cluster name	$E(B-V)$	r_{max} (arcsec)	g	i	$(g-i)_0$	M_V	$(V-I)_0$	r_h (pc)	Quality Flag	Notes
G1	0.057	32.6	14.17	13.23	0.77	− 10.79	0.95	8.7	B	s,b,m
G2	0.052	25.2	15.97	15.21	0.67	− 8.92	0.87	5.0	B	s
G339	0.093	11.8	17.47	16.55	0.75	− 7.58	0.94	5.3	A	–
G353	0.082	10.4	17.39	16.58	0.67	− 7.60	0.87	4.8	A	–
B514	0.058	25.2	16.02	15.17	0.77	− 8.91	0.95	6.6	A	–
B517	0.065	–	–	–	–	–	–	–	D	e,r*
EXT8	0.068	15.5	15.79	14.58	0.56	− 9.28	0.79	4.3	B	s
MGC1	0.086	37.4	15.60	14.15	0.71	− 9.59	0.91	8.8	A	–
H1	0.070	18.5	16.25	15.45	0.68	− 8.70	0.88	4.5	B	s
H2	0.059	18.5	17.43	16.60	0.73	− 7.50	0.91	5.2	A	–
H3	0.069	8.9	18.48	17.53	0.85	− 6.52	1.01	5.5	A	–
H4	0.073	17.0	17.17	16.28	0.74	− 7.82	0.93	5.4	A	–
H5	0.075	17.0	16.51	15.76	0.64	− 8.44	0.85	9.5	A	–
H7	0.057	17.0	17.76	16.92	0.73	− 7.17	0.92	10.5	A	–
H8	0.062	11.1	19.33	18.18	0.87	− 5.71	1.03	11.8	B	f
H9	0.055	–	–	–	–	–	–	–	D	e,x
H10	0.065	23.7	16.25	14.88	0.77	− 8.86	0.95	5.8	A	–
H11	0.071	11.8	17.10	16.23	0.75	− 7.88	0.93	4.1	A	–
H12	0.066	13.3	16.75	15.95	0.68	− 8.19	0.88	4.0	A	–
H15	0.057	11.8	18.46	17.20	0.62	− 6.60	0.83	10.3	A	c
H17	0.052	9.6	17.85	16.47	0.79	− 7.23	0.96	3.3	A	–
H18	0.087	14.8	16.92	16.08	0.70	− 8.09	0.90	4.1	A	–
H19	0.059	7.4	17.66	16.77	0.74	− 7.29	0.92	4.9	A	–
H22	0.050	11.1	17.26	16.43	0.74	− 7.65	0.93	4.2	B	g
H23	0.051	8.9	17.00	15.55	0.85	− 8.09	1.01	3.6	B	b,r
H24	0.098	14.8	17.97	17.04	0.75	− 7.10	0.94	8.9	A	–
H25	0.094	14.8	17.12	16.21	0.76	− 7.93	0.94	5.8	A	–
H26	0.053	14.8	17.66	16.34	0.70	− 7.40	0.90	5.6	A	–
H27	0.055	14.8	16.66	15.39	0.66	− 8.39	0.86	4.9	A	–
HEC1	0.060	12.6	19.06	18.39	0.65	− 5.82	0.86	15.7	A	–
HEC2	0.055	12.2	19.51	18.03	0.78	− 5.60	0.96	12.4	B	c,e,r
HEC3	0.070	15.5	19.63	18.71	0.83	− 5.36	1.00	17.6	A	c
HEC6	0.073	18.5	19.09	18.12	0.75	− 5.92	0.94	26.7	A	c
HEC7	0.087	16.7	18.48	17.53	0.82	− 6.57	0.99	19.5	A	c
HEC10	0.106	20.4	18.97	17.98	0.79	− 6.14	0.97	22.5	A	c
HEC11	0.048	8.9	18.41	17.03	0.70	− 6.65	0.90	14.6	B	c,g,r
HEC12	0.049	20.4	18.93	17.48	0.82	− 6.16	0.99	29.9	A	c
HEC13	0.048	13.7	19.48	18.27	0.64	− 5.54	0.85	20.7	B	c,e,r
B270D	0.087	6.7	17.77	16.86	0.76	− 7.26	0.94	6.6	B	f,r
SK213C	0.121	3.3	19.43	18.43	0.81	− 5.72	0.98	4.4	B	f,r
SK255B	0.070	8.1	18.01	17.00	0.89	− 7.01	1.04	5.6	B	b,f,r
SH06	0.168	8.1	16.43	16.55	− 0.49	− 8.45	0.00	9.9	A	–
SDSS1	0.068	8.1	18.33	17.22	0.95	− 6.71	1.10	12.0	B	m
SDSS3	0.066	6.7	19.06	17.95	1.03	− 5.98	1.16	7.2	A	–
SDSS6	0.079	–	–	–	–	–	–	–	D	e,x

Notes: b = nearby bright star, poorly masked or not maskable; c = centroided by eye; e = affected by CCD edge; f = high field star density; g = nearby bright galaxy, poorly masked or not maskable; m = masking required for many contaminating sources; r = restricted maximum aperture; r* = severely restricted maximum aperture; s = saturated at centre; x = missing in one or both filters.

(i) A. An ideal isolated cluster, with an unrestricted maximum aperture and limited or no masking of contaminant sources necessary.

(ii) B. Minor issues, such as the necessity for moderate masking of contaminants, or a slightly restricted maximum aperture due to a CCD edge, nearby bright star, or non-trivial field background – but not sufficient to underestimate the flux by more than ∼0.1–0.2 mag.

(iii) C. Major issues and potentially significant unreliability, due to, for example, scattered light from a very nearby bright star or galaxy, a strongly limited maximum aperture, or a contaminant coincident with the cluster centre, the masking of which interfered substantially with the cluster flux.

(iv) D. Fatal problems, such as the majority of the cluster falling off the edge of a CCD, or the centre falling precisely coincident with a bright contaminant that could not be masked. Useful photometry is not possible for objects in this category.

The quality flags are included in Table 6 along with notes indicating the specific issues, if any, arising for each particular GC (for example, whether r_{max} was truncated, and if so why). For any analysis

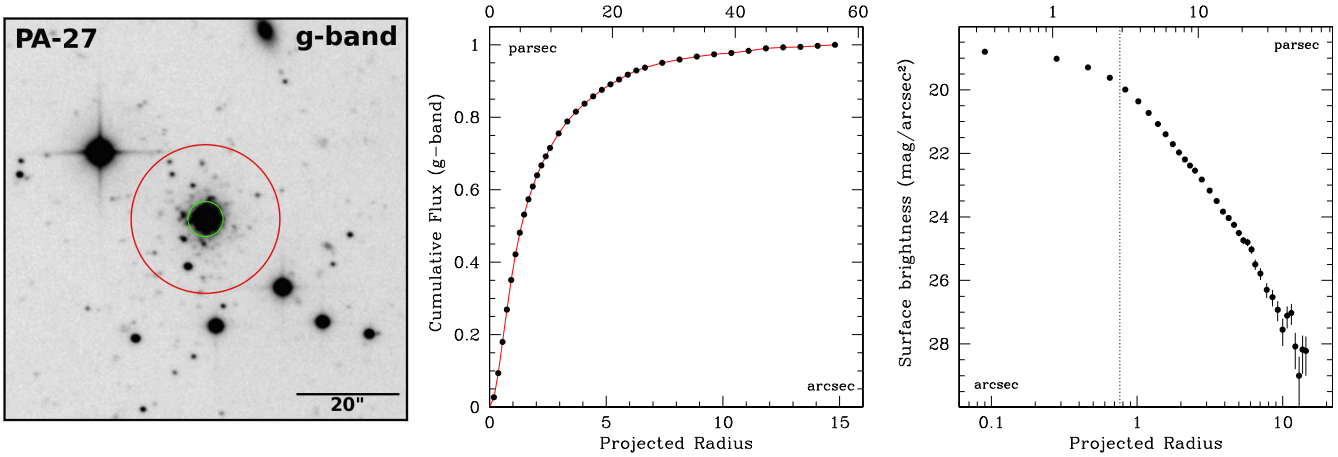

Figure 8. Example of our photometric measurements for PAndAS-27. The left-hand panel shows the g-band image of the cluster, with the maximum aperture ($r_{\rm max} = 14.8$ arcsec) marked in red, and the colour aperture (3.5 arcsec) marked in green. North is to the top of the page, and east to the left; the moderately bright foreground star within $r_{\rm max}$ to the SSE of the cluster was masked during the procedure. The PSF FWHM is slightly broader than the PAndAS g-band median at 0.76 arcsec. The central panel shows the curve-of-growth for PA-27; note that this has clearly levelled out by the time the maximum aperture is reached. The measured half-light radius is $r_{\rm h} = 1.4$ arcsec ~ 5.2 pc. The right-hand panel shows the curve-of-growth converted to a radial surface-brightness profile. The PSF FWHM is marked with a vertical dotted line; note that the profile flattens rather abruptly within this radius.

utilizing our photometric measurements, only objects in categories A and B should be used. Photometry for objects flagged with a C is useful only for determining indicative properties such as whether a cluster is 'bright' or 'faint', or 'compact' or 'diffuse'.

Because all the GCs for which we derived photometry are either brand new, or sit at large galactocentric distances, there is minimal overlap between our sample and the set of objects possessing high-precision luminosity measurements in the literature. We found eight compact category 'A' or 'B' clusters in our sample for which luminosities were measured from *HST* imaging by Tanvir et al. (2012) – H1, H4, H5, H10, H23, H24, H27 and B514. Because the *HST* imaging is in different filters than our PAndAS data, we compare the integrated absolute V-band luminosities, M_V, calculated from the total g- and i-band magnitudes as detailed in Section 5.4 below. The mean offset in M_V between our measurements and those from Tanvir et al. is $+0.09$ mag, and the dispersion about this value is 0.13 mag. Our luminosities are typically a little fainter than the *HST* measurements, which is not surprising as resolved photometry allows cluster members to be isolated even at radii well beyond our adopted $r_{\rm max}$ values.

We located four additional compact category 'A' or 'B' clusters in our sample that have previous luminosity measurements from *HST* imaging calculated by Barmby et al. (2007) – G1, G2, G339 and G353. When added to the Tanvir et al. clusters, the mean offset in M_V between our measurements and those from the literature drops to $+0.01$ mag, but the dispersion rises somewhat to 0.18 mag.

Finally, there are two very diffuse clusters in our sample that were measured by Tanvir et al. – HEC7 and HEC12. For these two objects, we find M_V to be more substantially underestimated, by 0.46 and 0.52 mag, respectively. It is not clear why our M_V estimates are $\sim$0.5 mag fainter than the *HST* values – most likely this reflects an inherent systematic limitation in integrating the extremely faint diffuse light component of these objects on medium-deep ground-based imaging.

5.2 Size estimates

In addition to determining the GC luminosities, we also used the curves-of-growth to obtain an empirical measure of their structures – as parametrized by the half-light radius $r_{\rm h}$, which is the projected radius of an aperture encircling half a cluster's flux. We report $r_{\rm h}$ for each GC in Table 6; this quantity for a given target is the straight average of the (independent) measurements from the g- and i-band images.[9] The quoted sizes are not meant to represent extremely precise measurements of the cluster structures – performing such work on distant objects such as these using ground-based imaging is challenging and complex, and beyond the scope of this paper. Rather, our estimates of $r_{\rm h}$ are intended to provide a quantitative indication of whether a GC is compact or diffuse, or somewhere in between. It has been known for some time that the halo of M31 hosts numerous unusually extended clusters (see e.g. Huxor et al. 2005; Hux11), and it is thus of interest to be able to examine, even if just at an indicative level, the distribution of GC sizes across the complete sample.

We first note that our method of estimating $r_{\rm h}$ is robust only if $r_{\rm max}$ falls on the flat part of the curve-of-growth. If not, then both the total luminosity and the half-light radius will be underestimated. As described above, clusters for which $r_{\rm max}$ was truncated are flagged in the table; quoted sizes for these objects should be treated with caution.

An additional, and arguably more important factor to consider is the effect of the seeing profile on our size measurements. Compact GCs in both the MW and M31 have $r_{\rm h} \sim 3-5$ pc (e.g. Harris 1996; Tanvir et al. 2012), which corresponds to an angular size of $\sim$0.8$-$1.3 arcsec at the M31 distance ($\mu = 24.47$). This is not much larger than the mean full width at half-maximum (FWHM) of point sources in PAndAS imaging, which is 0.67 arcsec in g and 0.60 arcsec in i. Thus, observations of $r_{\rm h}$ for very compact clusters in our sample largely reflect the seeing profile of the PAndAS image in which the object falls, rather than the intrinsic properties of the GC. In principle, this problem may be corrected by careful

[9] Although $r_{\rm h}$ may, in principle, be intrinsically slightly variable between various passbands (if, for example, a GC is mass segregated), in practice our individual measurement errors of $\gtrsim$10 per cent (see the text) are dominant. We take the mean of the two size estimates to try and minimize this random uncertainty.

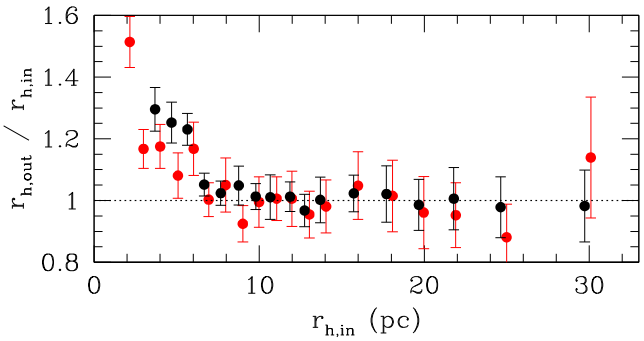

Figure 9. Measured versus input half-light radii for artificial clusters with luminosities $M_V \sim -8$ (black points) and ~ -5.5 (red points). For clarity, the black points have been offset slightly along the *x*-axis.

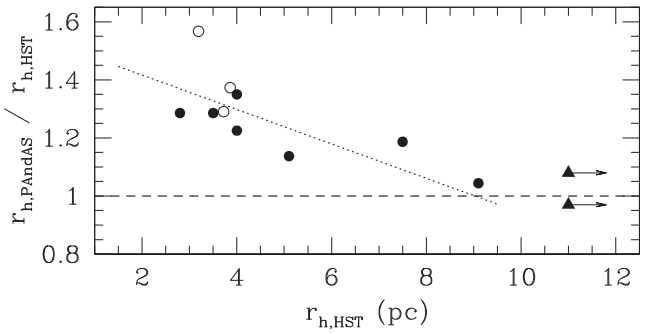

Figure 10. Half-light radii derived in this paper versus those derived from *HST* imaging by Barmby et al. (2007, open points) and Tanvir et al. (2012, filled points). Circles represent compact GCs, while triangles are diffuse GCs. Note that the two triangles should sit at ∼20 pc and ∼30 pc, but have been plotted at smaller radii to maintain clarity. The inclined dotted line represents a straight linear fit to all points in Fig. 9 for which the input size was below 9 pc. The apparently deviant point from Barmby et al. (2007) is G2, which is mildly saturated in our images (pushing r_h to a larger value). The point for G1 falls well off the top of the plot as it is quite strongly saturated in the PAndAS images.

deconvolution of the local image PSF and the radial brightness profile of the cluster; this problem will be addressed by an upcoming analysis of a substantial new *HST* data set (Mackey et al. in preparation). For now, we used artificial GC images generated to assess the completeness of our PAndAS catalogue (see Section 6) to explore the impact of the PSF on our size measurements.

We constructed two representative samples from the full suite of 4760 artificial GCs. As we describe in detail in Section 6, these objects were generated by first specifying a structure and luminosity, and then constructing a realistic image assuming the median PAndAS seeing. Both of our samples contained GCs spanning the full range of input half-light radii $r_h \sim 3-35$ pc, but for one ensemble the cluster luminosities fell within the range $M_V = -8.0 \pm 0.3$ and for the other within $M_V = -5.5 \pm 0.3$. We passed each artificial cluster in these two samples through our photometry pipeline. Note that we only selected objects that would have been classified in category 'A' in terms of the quality of the photometric measurement.

The results of this process are presented in Fig. 9. The marked error bar for a given size bin corresponds to the standard deviation in the measured GC sizes within that bin. It is clear that for GCs with input r_h larger than $\sim 8-10$ pc, we recover a very reasonable estimate of the object's size. This appears to be true irrespective of luminosity, although not surprisingly the scatter noticeably increases for lower luminosity GCs compared to higher luminosity GCs. Our tests indicate that typical uncertainties in the measured values of r_h are $\lesssim 8$ per cent for $M_V \sim -8$ objects and $\lesssim 12$ per cent for $M_V \sim -5.5$ objects. These uncertainties increase to ∼20 per cent for low-luminosity objects with very large r_h.

Below $r_h \sim 8$–10 pc, it is clear that the size measurements are significantly affected by the seeing profile, as expected. This limit corresponds to roughly three times the FWHM of the PSF used when constructing the artificial cluster images. It is interesting to note that while the measured r_h values become increasingly different from the input values when moving to smaller sizes, within the limitations of the scatter the ordering is preserved. That is, a GC that is intrinsically more compact than another will still be measured as such by our photometry pipeline even when strongly affected by the PSF. We must bear in mind that the seeing profile does vary between PAndAS images, unlike for our artificial clusters; however, as previously reported the rms scatter about the mean seeing values is small (∼0.1 arcsec).

We return briefly to the sample of 12 compact GCs and 2 diffuse GCs for which high-precision photometry and structural measurements exist in the literature. Fig. 10 shows a comparison between our r_h measurements and those derived from *HST* imaging by Barmby et al. (2007) and Tanvir et al. (2012). This strongly resembles Fig. 9 – for cluster sizes below $\sim 8-10$ pc, our estimated r_h values are clearly too large; however, the correct ordering is preserved. Indeed, our measurements appear to behave exactly as predicted by the artificial cluster tests – the inclined dotted line represents a straight linear fit to all points in Fig. 9 with input size below $r_h = 9$ pc, and this provides an excellent description of how strongly our measured quantities deviate from those obtained via *HST*. As a final note, we see that for the two diffuse clusters our r_h measurements match those from *HST* to better than ∼10 per cent, consistent with our estimated uncertainties.

5.3 Integrated colours

Comparing our *g*- and *i*-band flux measurements for a given GC allows us to derive the integrated colour of that object. In principle, we could calculate $(g - i)$ directly from the total luminosities measured within r_{max}. However, previous work has found that employing a smaller aperture can lead to a more robust result (e.g. Huxor et al. 2009; Veljanoski et al. 2013b). This is perhaps not too surprising, as the larger the aperture for colour measurement, the more sensitive the result is to (i) the presence of unidentified contaminants, and (ii) the accuracy of the estimated background level.

For this work, there are some subtleties associated with determining an optimal colour aperture. First, this methodology is predicated on the absence of intrinsic colour gradients within the target GCs. This appears reasonable – high-resolution studies from *HST* have not revealed any such gradients (e.g. Tanvir et al. 2012). Second, our catalogue spans a very large range of cluster sizes, so it does not make sense to simply apply a uniform colour aperture across the entire sample. A small aperture that might work well for a compact GC could lead to a very misleading result for a diffuse GC, as it would be extremely sensitive to the presence, or absence, of a handful of bright stars at the centre of such an object. Much better is to define an aperture that samples the same region in every cluster – for example, r_h; however, this introduces a third issue which is that, as we have already seen, compact GCs are strongly affected by the seeing profile. In the context of a colour measurement, it is important to recognize that any difference in the PSF width between the *g*- and *i*-band images leads to an artificial colour gradient at the centre of the object due to the differential redistribution of flux. If

the colour aperture is set to be too small, any such gradient will result in an erroneous measurement.

Fortunately, we already know from Fig. 9 the radius at which the effect of the seeing profile becomes negligible. Thus, we set the colour aperture to be equal to r_h for all GCs down to a conservative limit of $r_h = 3.5$ arcsec ∼13 pc; for any clusters with r_h smaller than this, the colour aperture is set at 3.5 arcsec. This lower limit matches the uniform colour aperture used in comparable studies, such as that of Veljanoski et al. (2013b) for GCs in the M31 dE companions NGC 147 and 185 (although note that that sample did not span anything like the range in size as does the present sample).

5.4 Photometric transformations

We conclude this section by summarizing the measurements reported in Table 6. For each GC, we list the foreground colour excess $E(B-V)$ as derived from the Schlegel, Finkbeiner & Davis (1998) maps, and the maximum photometry aperture r_{max}. Next, we list the total integrated g- and i-band AB magnitudes within r_{max}, along with the $(g-i)$ colour determined from a more central aperture as described above. The colour as reported has been dereddened using the appropriate coefficients from the study of Schlafly & Finkbeiner (2011):

$$g_0 = g - 3.303\,E(B-V)$$
$$i_0 = i - 1.698\,E(B-V)\,. \quad (1)$$

An important subtlety is that in mid-2007 the CFHT/MegaCam i-band filter was broken, and subsequently replaced with a new filter possessing a slightly different transmission profile. As a result, instrumental i-band magnitudes for GCs falling in images taken prior to 2007 June are calibrated to a slightly different system than for GCs taken after this date. To ensure a consistent set of measurements across the entire sample, we use the relationship from Ibata et al. (2014) to transform the photometry for GCs imaged with the old i-band filter on to the system of the new filter. Since all our objects have $(g - i_{old}) < 1.9$, this takes the form

$$i_{new} = i_{old} + 0.031\,(g - i_{old}) - 0.010\,. \quad (2)$$

To facilitate comparison with GCs in the inner parts of M31, as well as in systems belonging to other galaxies, we also list in Table 6 our photometry transformed to the standard Johnson–Cousins system using the relations from Hux08 (see also Veljanoski et al. 2013b). We first convert from AB magnitudes to Vega magnitudes:

$$g_1 = g + 0.092$$
$$i_1 = i_{old} - 0.401\,, \quad (3)$$

and then transform to V and I:

$$V = g_1 - 0.42\,(g_1 - i_1) + 0.04\,(g_1 - i_1)^2 + 0.10$$
$$I = i_1 - 0.08\,(g_1 - i_1) + 0.06\,. \quad (4)$$

Note that, as explicitly denoted in equation (3), these relations are valid only for photometry in the *old* i-band system. Thus, we transform all our measurements into this system using the inverse of equation (2) *prior* to implementing the above procedure. In Table 6, we list the absolute V-band magnitude M_V and the dereddened $(V-I)$ colour. We calculate these from V and I assuming a distance modulus $\mu = 24.47$, the relevant $E(B-V)$, and, as before, the appropriate coefficients from Schlafly & Finkbeiner (2011):

$$V_0 = V - 2.742\,E(B-V)$$
$$I_0 = I - 1.505\,E(B-V)\,. \quad (5)$$

6 SURVEY COMPLETENESS

A thorough, quantitative assessment of detection completeness is critical to the utility of our GC catalogue. We have identified two major sources of incompleteness associated with the PAndAS data and our search technique, and we quantify each of these below.

6.1 Incomplete spatial coverage

Although PAndAS does an excellent job of achieving uniform imaging of the M31 halo to $R_{proj} \approx 120-150$ kpc in all directions, there are myriad small gaps in its spatial coverage. These arise from two sources: (i) spaces between the first and second, and third and fourth rows of CCDs on the MegaCam focal plane, which were typically not filled in by the small telescope dithers employed during the observations; and (ii) imperfect tiling of the PAndAS mosaic.

In general, this spatial incompleteness is of no consequence for the primary goal of the PAndAS survey – studying the properties of the resolved M31 field halo and the large-scale substructures and overdensities that are found within it. Individual satellite dwarf galaxies of M31 are also typically large enough to span the missing regions. GCs, on the other hand, are sufficiently small on the sky that they can easily fall into a gap in the coverage and not be detected. We are aware of at least one such case of this occurring – the object H9 from Hux08, which sits at $R_{proj} = 56$ kpc and was originally discovered in INT/WFC observations, does not appear in any PAndAS image because it sits squarely in an inter-chip gap.

Fortunately, this kind of incompleteness is straightforward to quantify. It affects all GCs equally, irrespective of their morphology or luminosity; all that is required is to calculate the fraction of missing coverage as a function of projected galactocentric radius. To do this, for every PAndAS image we used the WCS information in the header to determine the coordinates of the four corners of each of the 36 CCDs and hence the equations defining their edges in RA and Dec. Note that we treated g- and i-band images independently in the list, as there are often small spatial offsets between images in the two filters and we only needed coverage from one filter to identify a GC.

Next, we constructed circular annuli about the M31 centre and filled each one with points generated at random positions so as to achieve uniform coverage of the area within the annulus. Each annulus was of width 0.5 kpc at the M31 distance, or 0.°0366 on the sky. We generated enough points per annulus to achieve a minimum density of 100 arcmin^{-2} – sufficient to properly sample the inter-row gaps between CCDs (∼80 arcsec wide). Using the complete list of CCD edge equations, we tested each point to see whether it fell within the area covered by any given chip, and hence within the imaged region of the PAndAS footprint. The fractional coverage for a particular annulus was then simply the ratio of imaged to total points generated inside that annulus.

Fig. 11 shows our results. In the central regions of M31, within $R_{proj} \approx 10$ kpc, there are sufficient overlapping images that the spatial coverage is complete. Beyond this, the coverage falls to ∼96 per cent all the way out to $R_{proj} = 105$ kpc, where the irregular edge of the PAndAS footprint gradually begins to affect the completeness. There is a shallow decline to ∼80 per cent coverage at

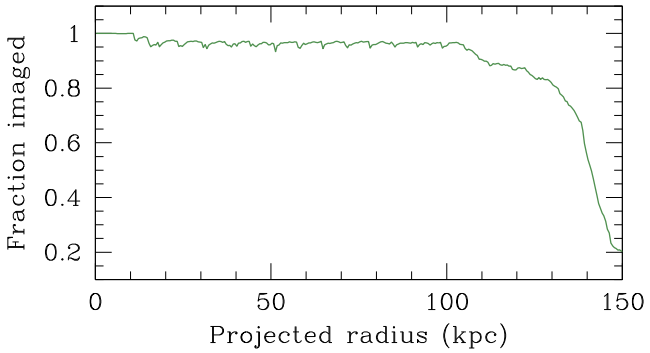

Figure 11. Fractional spatial coverage of the PAndAS survey imaging as a function of projected radius from the M31 centre.

$R_{\rm proj} = 130$ kpc, and then beyond this a rapid drop to ∼20 per cent coverage at 150 kpc.

How does this affect our GC sample? Including previously catalogued objects, we know of 82 GCs with projected radii in the range $25 \leq R_{\rm proj} < 105$ kpc; however, only 81 of these appear in PAndAS imaging (recall that H9 falls in an inter-chip gap). The 96 per cent spatial coverage over this radial range leads us to expect 84.4 GCs, so we are likely missing just 2 or 3. Given the radial decrease in the spatial density of GCs (Hux11; Mackey et al. in preparation), and the uniform level of areal incompleteness, these missing objects are more likely to lie at smaller rather than larger projected radii.

In the range $105 \leq R_{\rm proj} < 130$ kpc we know of 8 GCs, all of which appear in the PAndAS imaging. A crude integration of the completeness function suggests we are missing ∼1 additional GC in this range. Finally, in the range $130 \lesssim R_{\rm proj} < 150$ kpc, we have found only one cluster in the PAndAS imaging (Mackey et al. 2013b); there is probably $\lesssim$1 other similarly remote object that falls outside the survey footprint.

To summarize, we have plausibly missed ≈3−5 GCs over the range $25 \leq R_{\rm proj} < 150$ kpc due to the incomplete spatial coverage of the PAndAS imaging.

6.2 Cluster identification/recognition

The completeness of our catalogue is also affected by our ability to identify objects as GCs. That is, it is certain that we miss some clusters due to them being too small, faint, compact or diffuse (or some combination of these) to recognize as GCs. There is also the possibility of human error to consider – missing objects due to, say, a lapse in attention while searching images.

All indications suggest that human error is a negligible factor for our search. As a first pass, one of us (ADM) inspected ∼30 per cent of the images previously searched by APH, including a number with no GCs as well as some of those more heavily populated with GCs. In all cases, the consistency of the results was excellent, suggesting that our methodology, at least in uncrowded regions of low background, is robust. In addition to this, we recovered all known GCs in our primary search area ($R_{\rm proj} \geq 25$ kpc) – from both the RBC (Galleti et al. 2004) and the previous INT survey (Hux08) – with no omissions (barring H9). Finally, the automated search for dwarf spheroidal satellites of M31 devised by NFM (Martin et al. 2013) recovered just one missed GC across our entire survey area. This object (PA-31) is diffuse and very faint, falling near our 50 per cent completeness limit (see below) – so its original omission is not surprising. The search algorithm is sensitive only to objects possessing a sufficient number of resolved but relatively uncrowded stars. This describes just a relatively small fraction of our final GC catalogue, but includes bright objects such as MGC1 (e.g. Martin et al. 2006; Mackey et al. 2010a), as well as fainter extended clusters like PA-31. That it did not return a significant number of missed systems is another indication that human error has not introduced appreciable incompleteness into our catalogue.

To quantify how our ability to identify GCs in PAndAS imaging is affected by cluster luminosity and structure, we used a sample of artificial GCs. Ideally, these would be added into a wide variety of the PAndAS images themselves and then 'discovered' (or not) via a search methodology identical to that which we originally employed. This would have the added benefit of facilitating a more precise quantification of any incompleteness arising due to human error, as well as that due to the presence of very bright foreground stars (which we assume to be negligible due to the small number of such objects). Unfortunately, however, this technique is not practical. To achieve barely viable statistics requires a minimum sample approaching ∼5000 artificial clusters (see below). If distributed with comparable spatial density to the GCs in our catalogue, the necessary search area would total ∼50 times the area of the PAndAS footprint. Even distributing the artificial GCs with an unrealistic factor of 10 higher density would still require a search of several times the PAndAS footprint.

To circumvent this issue, we employed a simpler technique. We constructed small thumbnails with our artificial GCs at the centre, one per thumbnail, and then inspected each of these with the aim of determining, as objectively as possible, which would have been identified as a GC and which not. This methodology facilitated both our main aim of quantifying the faint limit of our survey, and our secondary aim of exploring how strongly this varies with cluster structure.

Under the assumption that incompleteness due to human error is negligible, there ought to be no difference between results derived from our simple inspection technique and those derived via a full search for artificial GCs. This assumption is a good approximation for luminous and/or compact GCs – objects which (i) were targeted by our inspection of colour–magnitude-selected candidates, and (ii) were typically prominent and thus easily located in the blind visual search. However, the approximation may break down subtly for objects of very low surface brightness because we knew, a priori, that each artificial thumbnail hosted an object at its centre. This is in contrast to the real situation where it was necessary to first find these objects in the blind search.[10] Ultimately, this mild systematic bias could mean that our derived faint completeness limits are too generous by a few tenths of a magnitude – and indeed, as we point out later, we may observe weak evidence for such an effect.

Our artificial clusters were generated across a binned grid in luminosity and concentration,[11] extending between the limits $-10 \leq M_V \leq -2$ and $0.5 \leq c \leq 2.5$. We generally adopted bin sizes of 0.25 mag in M_V and 0.1 in concentration, although for $M_V \leq -8$ and/or $c \geq 2.0$ we used bins of twice this size as finer discrimination was unnecessary. Within each bin we generated 10 artificial clusters with random M_V and c, in order to uniformly sample the bin. This resulted in a total ensemble of 4760 artificial GCs.

[10] Recall that diffuse clusters typically did not appear in the list of colour–magnitude-selected candidates.

[11] The concentration $c = \log(r_{\rm t}/r_{\rm c})$ where $r_{\rm t}$ is the cluster tidal radius and $r_{\rm c}$ the core radius, assuming a King (1962) model fit to the radial surface density profile. A concentration $c = 2.5$ typically indicates a GC affected by core collapse.

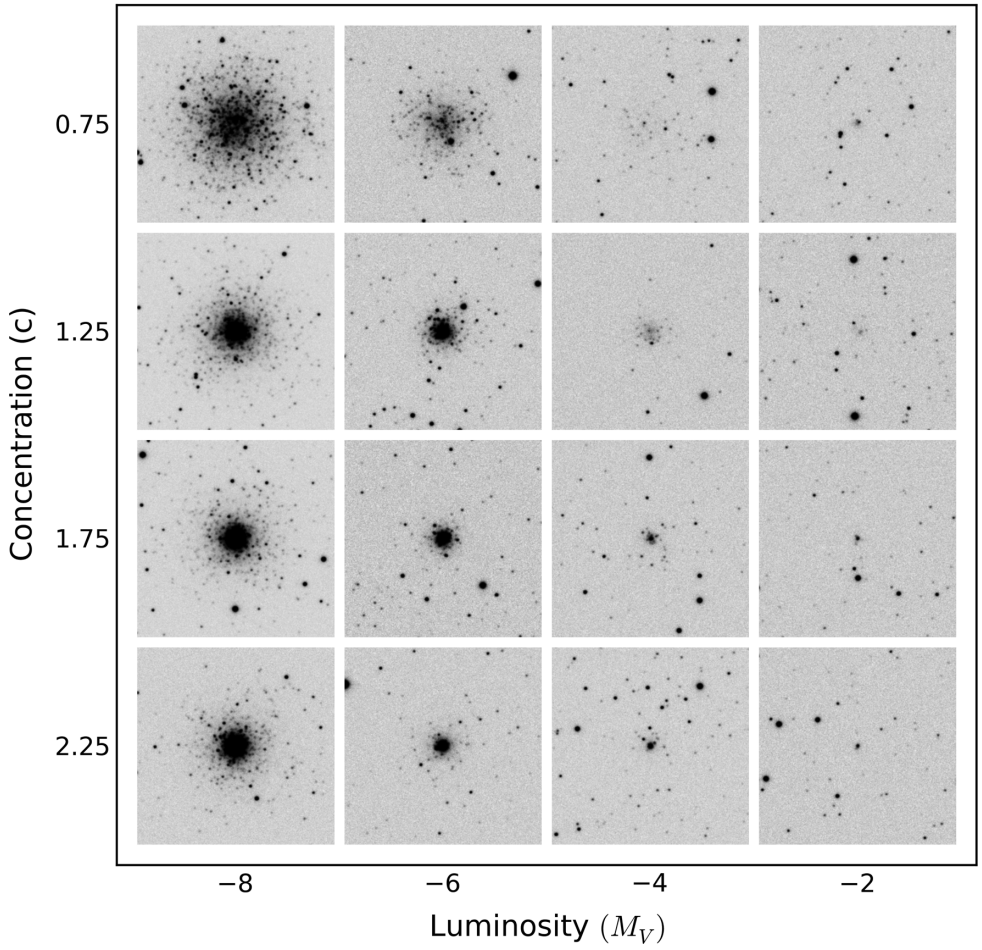

Figure 12. Examples of *g*-band artificial cluster images across the luminosity–concentration plane. These are central 1 arcmin × 1 arcmin cut-outs from our 1.6 arcmin × 1.6 arcmin thumbnails. Each assumes a stellar FWHM of 0.7 arcsec, typical for the vast majority of PAndAS *g*-band imaging.

We generated thumbnail images of these objects using the SIMCLUST software (Deveikis et al. 2008). This package generates a random realization of a GC given its age, metallicity, mass ($M_{\rm cl}$) and structural parameters ($r_{\rm c}$ and $r_{\rm t}$), and then 'observes' this model to produce a realistic image. For simplicity, we assumed a uniform age of 13 Gyr and metallicity of [Fe/H] = −1.8 for all our artificial clusters. These values are representative of those observed for metal-poor halo GCs in both the MW and M31 (e.g. Mackey et al. 2006, 2007; Marín-Franch et al. 2009; Dotter et al. 2010). Cluster masses were set from the randomly generated luminosities using $M/L = 2$, which is appropriate for the assumed age and metallicity. The structural parameters were determined by first assigning to each GC a random 3D galactocentric radius within $25 \leq R_{\rm gc} \leq 145$ kpc to match the range of projected radii observed for our PAndAS GC sample. This then defined the tidal radius according to the usual relationship $r_{\rm t} = R_{\rm gc}(M_{\rm cl}/M_{\rm g})^{1/3}$ where we assumed a galactic mass $M_{\rm g} = 1.2 \times 10^{12}\,{\rm M}_{\odot}$ for M31, and then our randomly generated concentration parameter determined $r_{\rm c}$. Given this set of input parameters, SIMCLUST randomly selects stars from an appropriate Padova isochrone (Marigo et al. 2008) according to a set mass function, until the desired cluster mass is reached. We used the segmented power-law mass function of Kroupa (2001) for our GCs. The stars are randomly distributed spatially according to a King (1962) model with appropriate $r_{\rm c}$ and $r_{\rm t}$.

SIMCLUST converts all stellar positions and luminosities for a given artificial GC to 'observed' quantities according to a specified distance and foreground extinction – we used $\mu = 24.47$, and the typical colour excess across the PAndAS footprint of $E(B-V) = 0.075$. These positions and luminositites are sent to the SKYMAKER software package (Bertin 2009), which generates the thumbnail images.[12] SKYMAKER also requires a model PSF, which we generated using the IRAF *psf* and *seepsf* tasks assuming a Gaussian profile of FWHM ∼0.7 arcsec, corresponding to the mean *g*-band stellar profile in PAndAS. We further specified the remainder of the SKYMAKER parameters to have values appropriate for CFHT/MegaCam and PAndAS. Finally, we also employed the ability of SKYMAKER to randomly add field stars across each thumbnail; we tweaked the relevant parameters to match, empirically, the range of field densities observed locally about our PAndAS GCs. Fig. 12 shows 1 arcmin × 1 arcmin central cut-outs from a handful of representative artificial GC images, across the luminosity–concentration plane.

Once all the artificial GC images had been generated, the order was randomized and the full set supplied to APH for inspection. To ensure a completely blind test, no accompanying information on individual cluster properties was provided. Once the inspection

[12] By default SIMCLUST provides *UBVRIJHK* magnitudes to SKYMAKER, which then produces images in these passbands. We made a small modification to the software in order to produce *g*-band magnitudes (and images), which we calculated according to the inverse of the transformation equations in Section 5.4.

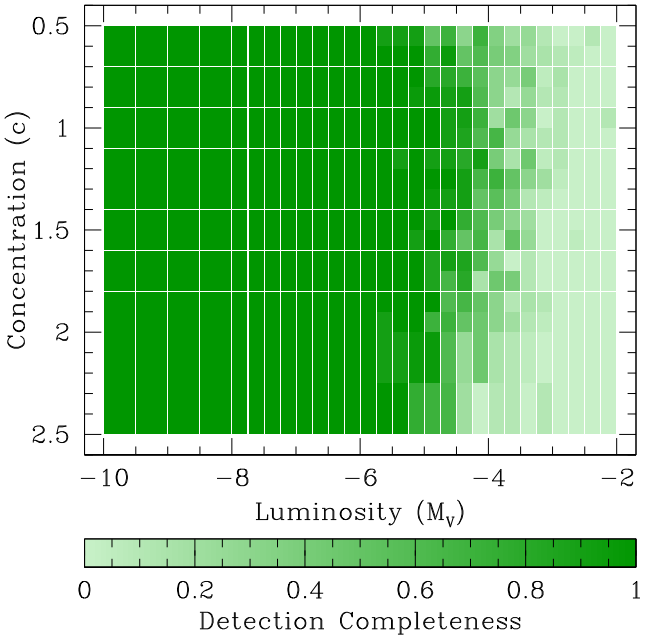

Figure 13. Detection completeness as a function of luminosity and concentration from our artificial cluster tests.

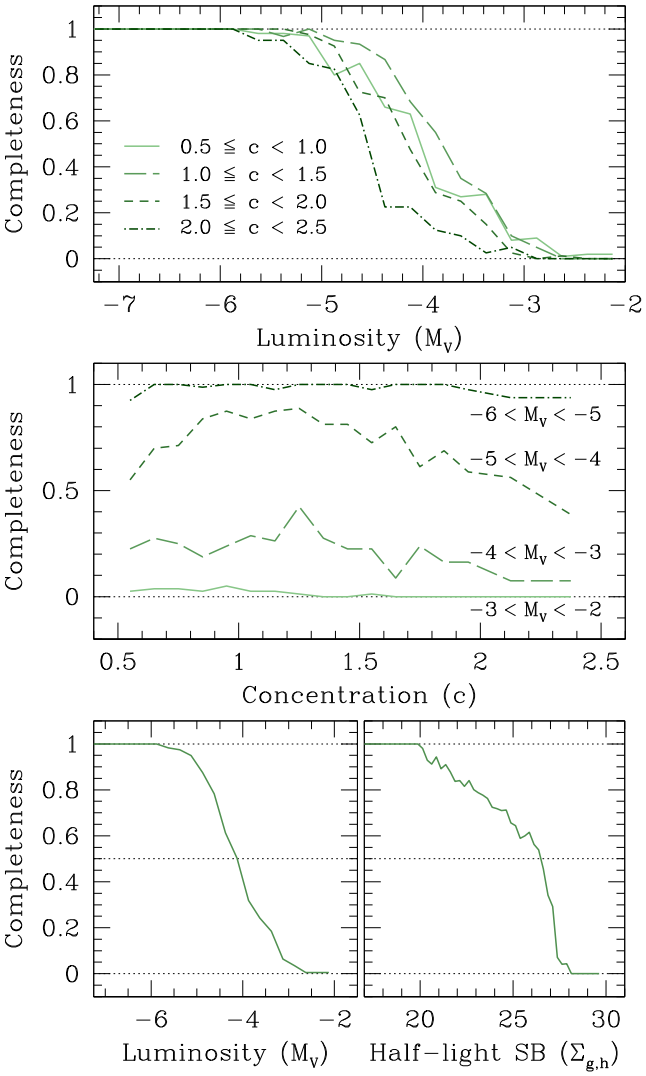

Figure 14. Upper panel: detection completeness as a function of cluster luminosity, collapsed into four concentration bins as marked. Middle panel: detection completeness as a function of cluster concentration, collapsed into four luminosity bins as marked. Lower panels: detection completeness across the entire sample of artificial clusters, as a function of luminosity (left) and g-band half-light surface brightness $\Sigma_{g,\mathrm{h}}$ in magnitudes per square arcsecond (right).

was complete, the classifications (a simple yes or no for each object) were returned to ADM for analysis. Figs 13 and 14 show the results. Our survey is complete to at least $M_V = -6$ irrespective of cluster structure; fainter than this, there is a weak but noticeable dependence on concentration. Peak detectability occurs for clusters with $c \sim 1.25$; there is a gradual fall-off for concentrations within ± 0.75 of this value, and a greater fall-off for very concentrated clusters with $c \geq 2$. Whereas our catalogue is >95 per cent complete down to $M_V \sim -5$ for GCs with $c < 2$, it is only ~80 per cent complete at $M_V = -5$ for objects with $c \geq 2$. The main reason for this is that, except for the most diffuse examples, GCs in PAndAS are predominantly recognizable as a group of resolved giant stars surrounding an unresolved, or partially resolved, core. For the most concentrated systems, the resolved halo vanishes with decreasing luminosity, leaving just a small central core that is indistinguishable from a foreground star or compact background galaxy. This effect is clearly visible in Fig. 12.

Considering the sample as a whole, our 50 per cent completeness level occurs at $M_V = -4.1$. The effect of differing cluster structures is to move this level by a few tenths of a magnitude in either direction about the mean value. The 50 per cent completeness levels for GCs with $0.5 \leq c < 1.0$ and $1.5 \leq c < 2.0$ match the mean level very closely. For those objects with $1.0 \leq c < 1.5$, the 50 per cent level moves somewhat fainter to $M_V = -3.8$, while for the most compact clusters with $2.0 \leq c < 2.5$ the 50 per cent level is substantially brighter at $M_V = -4.6$. Note that irrespective of structure, there is essentially no chance of detecting GCs with $M_V \gtrsim -3.2$ in PAndAS imaging. These limits are reflected in our real data, where our faintest GC has $M_V = -4.06$ (PA-45). Within the range $-4 < M_V < -3$, we expect to detect about 20 per cent of any clusters that are present (see the middle panel of Fig. 14). However, we found none – suggesting that (i) few such GCs exist in the halo of M31, and/or (ii) the PAndAS imaging data are somewhat more demanding than the synthetic GC data used to estimate the completeness and/or (iii) the mild selection bias we described above for very low surface brightness clusters has pushed our faint-end completeness limits too low by a few tenths of a magnitude.

It is informative to consider our completeness limits in terms of the half-light surface brightness $\Sigma_{g,\mathrm{h}}$ (that is, the mean g-band surface brightness within the cluster half-light radius r_h). Here, the fall-off is very sharp – our mean 50 per cent limit occurs at $\Sigma_{g,\mathrm{h}} = 26.5$ mag arcsec^{-2}, and there is essentially no chance of detecting clusters with $\Sigma_{g,\mathrm{h}} > 27.2$ mag arcsec^{-2}. Again, this ties in well with our detections. We have just one GC with $\Sigma_{g,\mathrm{h}} \approx 27$ mag arcsec^{-2} (PA-03), and only another four with $\Sigma_{g,\mathrm{h}} \gtrsim 26$ mag arcsec^{-2}. As usual, we are assuming $\mu = 24.47$ for M31, and a typical foreground extinction of $E(B-V) = 0.075$. Under such assumptions, our surface brightness limits recast in terms of V (i.e. $\Sigma_{V,\mathrm{h}}$) would be ~0.35 mag arcsec^{-2} brighter. Note that it is unnecessary to consider the effect of cluster structure on these limits because the faint end of the function ($\Sigma_{g,\mathrm{h}} > 26$ mag arcsec^{-2}) samples only diffuse ($r_\mathrm{h} > 10$ pc) and relatively low luminosity ($M_V > -6$) GCs.

7 RESULTS AND ANALYSIS

In this section, we explore the properties of the enlarged M31 halo GC system, using the new clusters described above and exploiting our analysis of completeness which was not available in any of our previous work (e.g. Hux11). As in Hux11, we study the ensemble photometric properties of the M31 GC system and compare them to those of the GC system of the MW. When taking photometry and structural measurements from this paper, we only include those clusters which have a quality flag of either 'A' or 'B' (see Table 6). We also exclude the two candidate GCs from our analysis.

In the analysis that follows, we supplement our catalogue of outer halo GCs with confirmed GCs from the most recent revision of the RBC (almost all of which are at $R_{\rm proj} < 25$ kpc). Since Hux11, there have been a number of significant changes to the RBC – Hux11 used version 3.5, and this has now been updated to version 5. In particular, the latest version adds the photometry of Fan et al. (2010) and Peacock et al. (2010), and the spectroscopy of Caldwell et al. (2009).

The sample of M31 GCs we take from the RBC is defined in a manner comparable to that used in Hux11, and exploits a number of flags provided in the RBC that help classify the characteristics of the GCs. We only use those objects for which the RBC flag 'f' is set to either 1 or 8 (indicating confirmed compact and extended GCs, respectively – the extended clusters all appear to be old metal-poor systems, so we treat them equally). We thus effectively exclude all objects in the RBC V5 that do not have imaging or spectroscopy confirming their status as GCs. M31 possesses a population of younger clusters, predominantly set against the galactic disc, which we also exclude as there are no comparable clusters in our MW sample. This was achieved by ensuring the flag 'yy' is 0 – indicating clusters that are 'not young' according the data of Fusi Pecci et al. (2005), based on the $(B - V)$ colour or the strength of the Hβ spectral index. Additional young clusters are excluded by removing objects for which the flag 'ac' is 1 or 2 (which indicate an age estimate of less than 1 Gyr, or $\sim$1–2 Gyr, respectively, drawing on the spectroscopy of Caldwell et al. 2009); and for which the flag 'pe' is not 0, 1 or 2 (based on Peacock et al. 2010, who use broad-band colours to identify likely young clusters).

These selection criteria leave a sample of 425 GCs from the RBC V5, which is actually fewer than the RBC V3.5 sample employed in Hux11 even though the catalogue now includes the 40 new GCs we presented in that paper. This reduction is due to the large number of objects that are either now known not to be GCs, or are now classified as being 'young'.

Many of the GCs in version 5 of the RBC also have new $E(B - V)$ values compared to version 3.5. In addition to those of Fan et al. (2010), which were available for Hux11, new values have been derived by Caldwell et al. (2011) from their spectroscopy. If any particular GC is in both Fan et al. (2010) and Caldwell et al. (2011), we take the mean of the two $E(B - V)$ values given for that cluster. If a GC within 25 kpc of the centre of M31 has no colour excess from either of these sources, we apply an average value of $E(B - V)$ derived from the medians of both samples. However, for those GCs with $R_{\rm proj} > 25$ kpc, we use the $E(B - V)$ values derived from the Schlegel et al. (1998) dust maps, as additional internal M31 reddening towards these objects is probably negligible. Note that we employ the updated reddening values from Schlafly & Finkbeiner (2011) as listed in Table 6.

Data on the MW GC system have also been updated since Hux11 was written. We now use the current version (dated 2010 December) of the McMaster catalogue (see Harris 1996),[13] although there are no major changes since the previous catalogue. In the analysis that follows we focus on the photometric properties of the GCs, derived from their observed magnitudes and colours. With this in mind, we exclude from our plots the 28 (of 157 total) MW GCs listed in the McMaster catalogue as having $E(B - V) > 1.0$, as A_λ is not constant at high extinction. These objects are, in any case, almost all rather poorly studied.

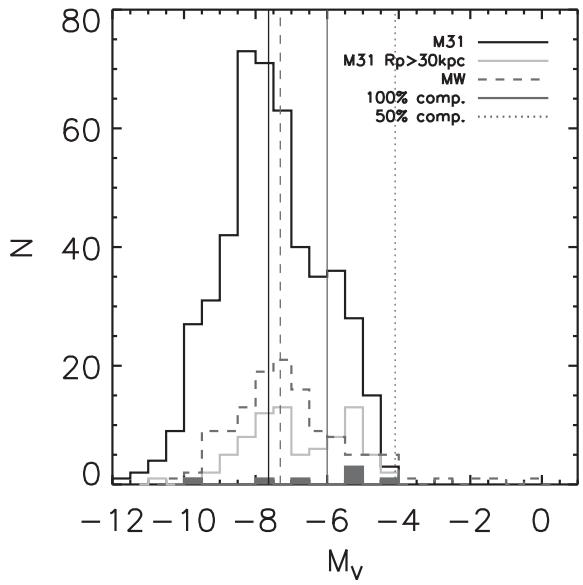

Figure 15. Histogram of M_V, showing the distribution for all M31 GCs, taking the additions and updates from this paper into account (black solid line), and the M31 GCs with a projected galactocentric radius $R_{\rm proj} > 30$ kpc (green solid line) compared to the MW (red line). The solid black and dashed red vertical lines indicate the median values for the M31 and MW GC systems, respectively. The solid red regions show the GCs associated with the Sagittarius dwarf galaxy. The completeness limits for our PAndAS GC search are also shown (blue vertical lines).

Analysis of the spatial layout of the M31 GCs, and their relationship to stellar substructures in the halo, will be addressed in detail in an accompanying paper in this series (Mackey et al. in preparation).

7.1 GC luminosity function

The M31 GC luminosity function (GCLF) is shown in Fig. 15. The median value of M_V for M31 is -7.6, compared to the -7.9 that we found in Hux11; that for the MW sits at -7.3, the same as in Hux11 despite the various minor updates to the McMaster catalogue.

In Hux11, we suggested that the then available data indicated a secondary peak in the M31 GCLF at $M_V \sim -6$ mag, although we noted at the time that many of the objects identified by Kim et al. (2007) as clusters were near this magnitude, but had questionable classifications. We further found that the secondary peak was visible when both inner halo ($R_{\rm proj} < 25$ kpc) and outer halo ($R_{\rm proj} > 25$ kpc) GCs were considered separately, suggesting that this might indeed be a real feature.

The new data reveal a more complex situation. With the updated RBC, the second peak for the full M31 sample (black histogram) no longer appears. This is primarily due to the reclassification of many of the Kim et al. (2007) GCs as stellar contaminants

[13] http://www.physics.mcmaster.ca/Globular.html

(Peacock et al. 2010), which reduces the number of confirmed GCs in this magnitude range. However, if we consider only the outer halo clusters (in this case $R_{\rm proj} > 30$ kpc), shown in green in Fig. 15, a bimodality in the GCLF is very clear with peaks at ~ -7.5 and ~ -5.5. The fainter secondary peak sits between our 100 per cent and 50 per cent completeness limits. Hence, it is possible that additional GCs exist around this luminosity, that we have not detected. These would further increase the prominence of the feature, and the location of the peak may shift slightly (probably towards slightly fainter magnitudes).

It is natural to ask about the typical nature of the GCs residing in the secondary peak. Mackey et al. (2010b) argue that a substantial fraction (perhaps up to ∼80 per cent) of the M31 GCs with $R_{\rm proj} > 30$ kpc have been accreted into the M31 halo along with their parent dwarf galaxies. Hence, the fainter peak in the GCLF, which is prominent only for the outer halo system, might well be primarily driven by the presence of this type of GC.

This scenario finds additional support if we consider the MW GCs that are believed to be associated with the Sagittarius dwarf galaxy (Law & Majewski 2010). Although there are only perhaps eight such GCs (Arp 2, NGC 6715, NGC 5634, Terzan 7, Terzan 8, NGC 5053, Pal 12 and Whiting 1), five of these have luminosities fainter than $M_V = -6$. More generally, Mackey & van den Bergh (2005) found a similar fainter peak in GCLF of the 'young halo' GCs of the MW, which they argued (from indirect evidence) are most likely accreted objects.

The M31 halo GCs near the secondary peak in the GCLF differ in other ways. A plot of M_V against $r_{\rm h}$ for the M31 GCs beyond 30 kpc (Fig. 16) shows that clusters with a luminosity near the fainter peak of the GCLF span a very broad range of half-light radii, while clusters near the more luminous peak are primarily compact.

Our GCLF for the outer M31 halo suggests that there is a substantial population of luminous GCs outside $R_{\rm proj} = 30$ kpc. A plot of absolute magnitude against projected radius (Fig. 17) makes this more explicit – our new PAndAS GC search has yielded many more luminous clusters in the outer halo compared to Hux11. Note that the MW GCs are plotted with an 'average projected distance', via

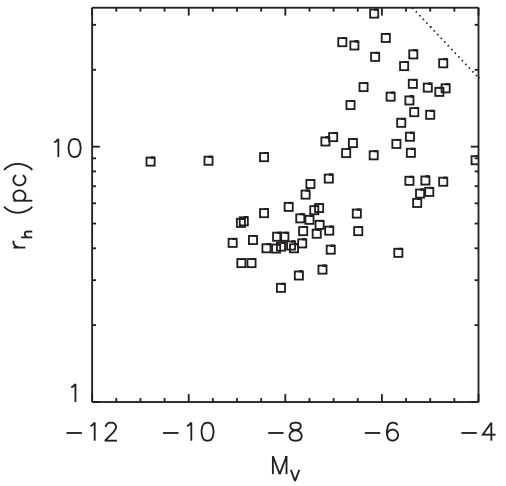

Figure 16. Plot of M_V against $\log_{10}(r_{\rm h})$ for M31 GCs in the outer halo, with a projected distance greater than 30 kpc. The more luminous clusters ($M_V < -7.5$) are relatively compact, whilst the fainter clusters span a broad range of effective radii. Recall that size measurements for any GC with $r_{\rm h} \lesssim 8-10$ pc are upper limits. The dashed line shows the location of our 50 per cent completeness limit.

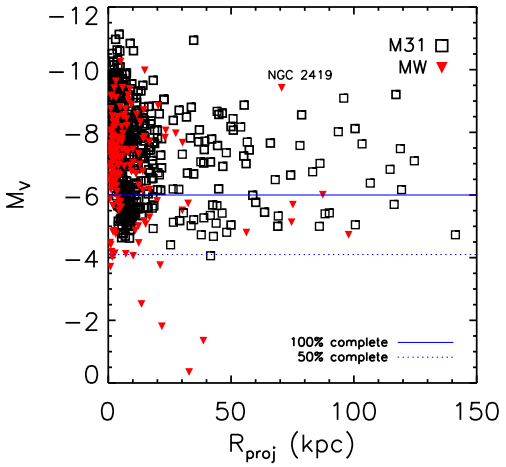

Figure 17. Plot of M_V against projected galactocentric radius $R_{\rm proj}$, with the completeness limits of our PAndAS search again shown (blue). In the case of the MW GCs, the actual distance ($R_{\rm gc}$) in this, and subsequent plots, is converted to an 'average projected distance' via the relationship $R_{\rm proj} = R_{\rm gc} \times (\pi/4)$. There are many luminous GCs in M31 at large radii, but a similarly abundant population is not seen in the MW.

the relationship $R_{\rm proj} = R_{\rm gc} \times (\pi/4)$, to make the published Galactocentric distances more directly comparable with the projected values of the M31 GCs. The number of luminous GCs at large galactocentric radii is in striking contrast to the situation seen in the MW. The only GC in the MW which is comparably luminous and also at a large distance from the Galactic Centre is the unusual object NGC 2419.

There is a population of very low luminosity clusters ($M_V > -4$) in the MW, which we would likely not see in the PAndAS data – if they were present – as at the M31 distance they lie well below our 50 per cent completeness limit. However, in the MW, these faint GCs are found at moderately large (projected) galactocentric radii, suggesting that deeper imaging in the future may indeed reveal such objects in the halo of M31.

7.2 GC colour distribution

The distribution of $(V - I)_0$ colours (Fig. 18) shows almost no difference to that found by Hux11. The median $(V - I)_0$ values for GCs in M31 and the MW are almost indistinguishable at 0.95 and 0.93, respectively.

When viewed as a function of galactocentric radius (Fig. 19), the results are again similar to those reported by Hux11. In that paper, we found a flat colour–radius relation for GCs in the outer halo. The new data are consistent with this, exhibiting only a marginal slope of -0.0007 ± 0.0004 mag kpc^{-1} for the GCs beyond 30 kpc. This uncertainty is reflected in spectroscopic results for a limited subset of M31 halo GCs, under the assumption that changes in integrated colour are largely a result of changing metallicity. Fan et al. (2011) found a small gradient (to decreasing metallicity at larger galactocentric distances) for GCs with $R_{\rm proj} > 25$ kpc, while Colucci, Bernstein & Cohen (2012) find a nearly constant metallicity for GCs with $R_{\rm proj} > 20$ kpc. Both these studies used previously published GCs, and although their sample extend to over 100 kpc, they have very few clusters in the distant halo. Our data greatly increase the sample size, improving the robustness of the result.

It is noticeable that although the $(V - I)_0$ colours of the full M31 and MW GC systems are almost identical, for the outer halo the MW GCs typically appear slightly redder than the bulk of the M31

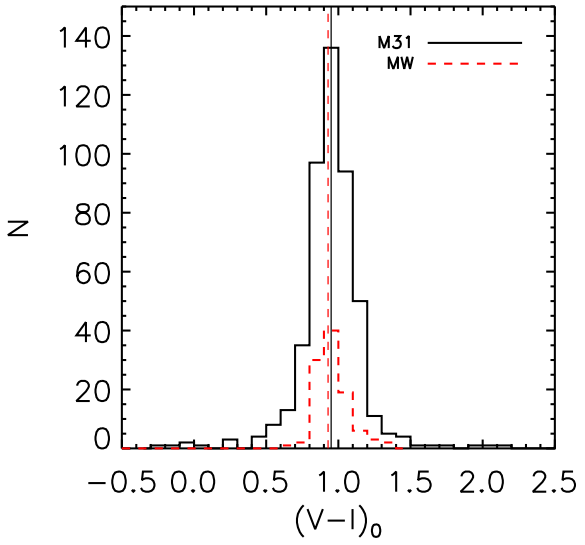

Figure 18. Histogram of $(V - I)_0$. The vertical lines show the median values for the full sample (solid) and the MW (red).

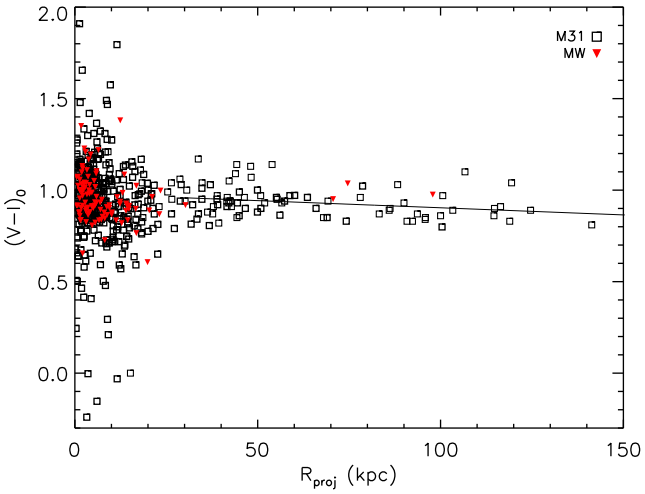

Figure 19. Plot of $(V - I)_0$ against R_{proj}. The black line shows a linear fit to the M31 GCs with $R_{proj} > 30$ kpc.

GCs at a comparable distance – although as there are very few MW GCs at these large galactocentric radii, it is difficult to draw firm conclusions.

7.3 Cluster sizes

One result that differs significantly from that seen by Hux11 concerns the distribution of half-light radii for outer halo M31 GCs. In Hux11, we suggested this may take a bimodal form, with one peak corresponding to the typical sizes of traditional compact GCs ($r_h \sim 3-5$ pc) and the other at much larger $r_h \gtrsim 15$ pc. Wang & Ma (2013) also reported a size bimodality for M31 GCs at $R_{proj} > 40$ kpc, but they used a small sample of clusters from Hux08 which were also included in our Hux11 analysis. We can now address this question definitively with our larger halo GC sample.

For comparison purposes, we also assemble a set of (inner) M31 GCs with recent size measurements in the RBC. The largest RBC

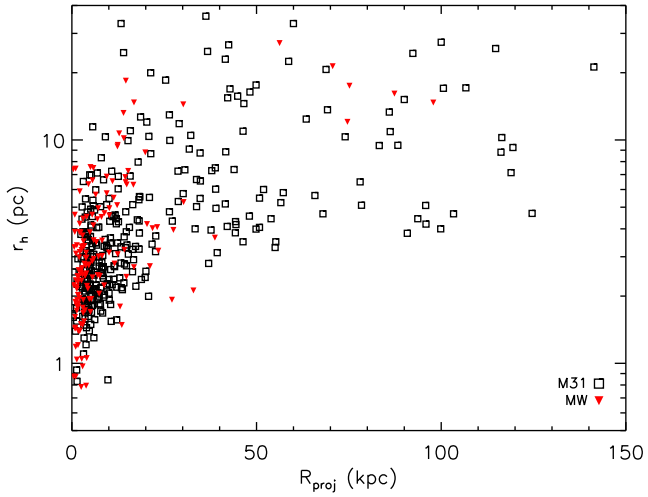

Figure 20. Plot of $\log_{10}(r_h)$ against R_{proj}. There is an apparently continuous range of half-light sizes at large galactocentric radii.

sample comes from the compilation of Peacock et al. (2009, 2010), which we supplement with measurements from Barmby et al. (2007) when only the latter is available. Note that Peacock et al. (2009) provided a careful demonstration that their GC size measurements showed excellent consistency with those derived from *HST* imaging by Barmby et al. (2007).

We remind the reader of the reliability of our determination of cluster effective radius as described in Section 5. For clusters smaller than $r_h \sim 8-10$ pc, the size measurements are significantly affected by the seeing profile (see Fig. 9), and we thus overestimate their values, typically by $\approx 20-30$ per cent. However, the relative ordering of such GCs by size ought to be largely correct. As described previously, some of the GCs we report measurements for in Table 6 also have sizes measured from *HST* imaging by Tanvir et al. (2012). We take these in preference where available, to try and minimize the effects of this issue.

In Fig. 20, we show r_h for M31 and MW GCs against projected distance from the centre of their host galaxy. The apparent bimodality in cluster size at large galactocentric radii for M31 GCs, as noted in Hux11, has now vanished. There are many clusters with r_h between 5 and 20 pc, in which range the size distribution appears rather evenly spread at all galactocentric radii outside ∼10 kpc. The original observation of bimodality may have been partly due to the difficulty in measuring accurate GC sizes from our INT/WFC data. We observe significant changes in the inferred sizes of some objects moving to the superior PAndAS data – for example, the clusters H7, H8 and H15 went from our default value for 'compact' GCs of 4.5 pc, used in Hux11, to ∼10 pc, while by contrast, some of the more extended clusters have smaller sizes measured from the PAndAS data than those obtained by Hux11.

The apparently even spread of cluster sizes larger than ∼5−10 pc in the M31 halo strongly suggests that the extended clusters first identified by Huxor et al. (2005) are simply objects selected from the upper tail of the GC size distribution. This is consistent with their constituent stellar populations, which appear indistinguishable from those observed in typical metal-poor compact GCs (see e.g. Mackey et al. 2006, 2007). It is also noticeable from Fig. 20 that the largest clusters observed in the remote MW halo are comparable to the sizes of many of the more extended clusters in M31 – that is, there do appear to be a few counterparts of the M31 extended clusters

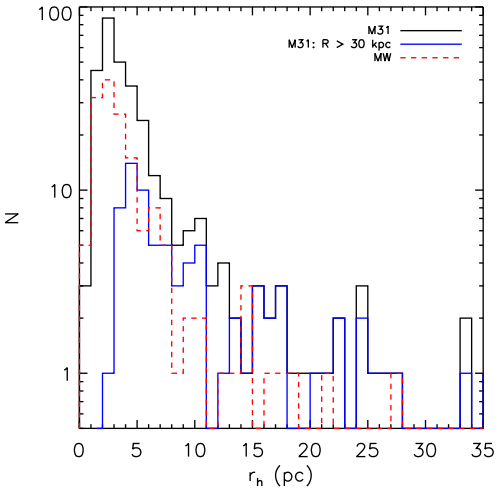

Figure 21. Histogram (logarithmic in N) of r_h. For large galactocentric radii (blue line), the distribution of half-light radii is considerably flatter than for the full M31 sample.

seen in the MW halo. The largest M31 clusters have greater r_h than any GCs found in the MW halo, but this is perhaps not surprising given the much more numerous M31 halo GC population.

Fig. 21 shows a histogram of r_h for M31 and MW GCs. Those for the full systems appear to share a very similar shape. However, it is notable that the distribution of r_h for M31 GCs with a galactocentric distance >30 kpc is quite unlike that for the full M31 sample. Even taking into account the tendency for our PAndAS measurements to overestimate the sizes of GCs with $r_h \lesssim 8$–10 pc, the distribution of half-light radii for clusters more than 30 kpc from M31 would still be considerably flatter than that of the full sample. That is, the ratio of the number of GCs with r_h above 8−10 pc to those with r_h below this level is substantially greater for M31 GCs with $R_{proj} > 30$ kpc than for the full M31 sample. A similar pattern is seen in the MW, albeit at lower significance due to the smaller numbers of clusters involved (e.g. Mackey & Gilmore 2004; Mackey & van den Bergh 2005). It is unclear to what extent this situation reflects the lower tidal fields in the outer regions of M31 (and indeed the MW), or whether it is due to the likely origin of many of these GCs in accreted dwarf galaxies (see also the discussion in Da Costa et al. 2009; Hwang et al. 2011).

8 CONCLUSIONS

In this paper, we present the final catalogue of M31 halo GCs from the PAndAS survey. Of these, 57 were identified by our usual method of visually searching the new image data, and one further cluster was found by a code searching for faint dwarf galaxies. Our catalogue represents the first detailed and uniform census of GCs across nearly the full extent of the M31 halo. We find numerous clusters with very large projected galactocentric radii ($R_{proj} \gtrsim 100$ kpc), reflecting the huge spatial extent of the M31 GC system.

We located a few additional GCs by revisiting outer halo candidates listed in the RBC. We found that three such candidates are indeed GCs, while one is an H II region with a possible embedded young cluster; and we also located one further new discovery that serendipitously falls near a star that was the source of the RBC entry. In addition, we found that three 'definite' outer halo GCs listed in the RBC are not clusters after all. Finally, we confirm that 10 of the 17 'high-confidence' SDSS clusters listed by dTZZ13 are indeed GCs, based on our higher quality PAndAS imaging. However, only one of their 42 'candidate' objects that we were able to examine was found to be a cluster.

Experiments with artificial clusters suggest that our GC survey is complete down to a cluster luminosity of $M_V = -6.0$, and has 50 per cent completeness limit at roughly $M_V \approx -4.1$. Our analysis indicates that an additional ∼3−5 clusters may lie undiscovered within the area covered by PAndAS imaging (i.e. within ≈150 kpc of M31), due to small gaps in the survey coverage. We cannot rule out that there may also be many very faint clusters with $M_V \gtrsim -4$ that we are unable to detect using PAndAS.

We used the PAndAS imaging to measure luminosities, colours and sizes for all known M31 GCs outside $R_{proj} = 25$ kpc. The results of this process confirm most of the findings from Hux11 with a much larger sample. The bimodality of the LF constructed using M31 halo GCs with $R_{proj} > 30$ kpc is perhaps the most notable feature. This bimodality is not seen in the LF constructed using more central clusters, and we suggest it may be a consequence of the dwarf galaxy accretion history of the outer M31 halo. The colours of the halo GCs show only a marginally significant shallow gradient with projected radius, while the distribution of half-light radii for the M31 halo GCs reveals an apparently continuous spread of cluster sizes, rather than the bimodality suggested by previous studies that used much smaller samples and shallower imaging.

Many of the new GCs described here have already been followed up by the PAndAS collaboration. For example, a large fraction of these objects is included in the studies of Veljanoski et al. (2013a) and the companion paper to this work by Veljanoski et al. (2014), where radial velocities have been used to explore the kinematics of the M31 outer halo GC system.

Individual clusters have also proved of interest. In Mackey et al. (2013a), we investigated two of the new PAndAS GCs (PA-7 and PA-8), which are almost certainly associated with a prominent halo substructure known as the South-West Cloud (see Lewis et al. 2013; Bate et al. 2014). These objects appear to be at least 2 Gyr younger than the oldest MW GCs, and thus fit with the trends identified by Perina et al. (2012), and show strong similarities to the supposedly accreted 'young halo' clusters in the MW (Mackey & van den Bergh 2005).

Our new clusters also provide a substantial number of GCs which exhibit properties unlike those studied in the MW. Examples include the few very most extended clusters, and the luminous, compact clusters found in the far halo of M31. Some of the new GCs may be of major interest. For example, PA-48 has a structure and ellipticity that may be more akin to a very faint dwarf galaxy than a typical GC (see Mackey et al. 2013b).

HST imaging reaches to below the horizontal branch at the distance of M31 in a just a couple of orbits – although it is a challenge to go much deeper. Brown et al. (2004) required a total of 3.5 d of exposure time to reach to 1.5 mag below the old main-sequence turn-off of the M31 GC SKHB 312. However, this situation will change with the launch of *JWST*, which should be able to reach the main–sequence turn-off for M31 GCs with manageable exposure times, allowing us to investigate the GC system of M31 in a manner comparable to our current understanding of the Galactic GC system. With low contaminating backgrounds, the GCs presented here will be ideal targets for such studies.

ACKNOWLEDGEMENTS

We would like to thank the referee, Flavio Fusi Pecci, for a detailed and constructive report that helped improve this paper. We also appreciate the careful reading by Luciana Federici and Silvia Galleti.

ADM is grateful for support by an Australian Research Fellowship (Grant DP1093431) from the Australian Research Council. AMNF, APH and ADM acknowledge support by a Marie Curie Excellence Grant from the European Commission under contract MCEXT-CT-2005-025869, during which this work was initiated.

This work is based on observations obtained with MegaPrime/MegaCam, a joint project of CFHT and CEA/DAPNIA, at the Canada–France–Hawaii Telescope (CFHT) which is operated by the National Research Council (NRC) of Canada, the Institute National des Sciences de l'Univers of the Centre National de la Recherche Scientifique of France and the University of Hawaii.

REFERENCES

Alves-Brito A., Forbes D. A., Mendel J. T., Hau G. K. T., Murphy M. T., 2009, MNRAS, 395, L34
Barmby P., Huchra J. P., 2001, AJ, 122, 2458
Barmby P., Huchra J. P., Brodie J. P., Forbes D. A., Schroder L. L., Grillmair C. J., 2000, AJ, 119, 727
Barmby P., McLaughlin D. E., Harris W. E., Harris G. L. H., Forbes D. A., 2007, AJ, 133, 2764
Bate N. F. et al., 2014, MNRAS, 437, 3362
Battistini P., Bonoli F., Braccesi A., Federici L., Fusi Pecci F., Marano B., Borngen F., 1987, A&AS, 64, 447
Bertin E., 2009, Mem. Soc. Astron. Ital., 80, 422
Brown T. M., Ferguson H. C., Smith E., Kimble R. A., Sweigart A. V., Renzini A., Rich R. M., VandenBerg D. A., 2004, ApJ, 613, L125
Caldwell N., Harding P., Morrison H., Rose J. A., Schiavon R., Kriessler J., 2009, AJ, 137, 94
Caldwell N., Schiavon R., Morrison H., Rose J. A., Harding P., 2011, AJ, 141, 61
Chies-Santos A. L., Larsen S. S., Kuntschner H., Anders P., Wehner E. M., Strader J., Brodie J. P., Santos J. F. C., 2011, A&A, 525, A20
Cockcroft R. et al., 2011, ApJ, 730, 112
Colucci J., Bernstein R. A., Cohen J., 2012, Proc. XII Int. Symp. on Nuclei in the Cosmos, available at: http://pos.sissa.it/cgi-bin/reader/conf.cgi?confid=146
Conn A. R. et al., 2012, ApJ, 758, 11
Crampton D., Cowley A. P., Schade D., Chayer P., 1985, ApJ, 288, 494
Da Costa G. S., Grebel E. K., Jerjen H., Rejkuba M., Sharina M. E., 2009, AJ, 137, 4361
Deveikis V., Narbutis D., Stonkutė R., Bridžius A., Vansevičius V., 2008, Balt. Astron., 17, 351
di Tullio Zinn G., Zinn R., 2013, AJ, 145, 50 (dTZZ13)
Dotter A. et al., 2010, ApJ, 708, 698
Elson R. A., Walterbos R. A. M., 1988, ApJ, 333, 594
Fan Z., Ma J., de Grijs R., Zhou X., 2008, MNRAS, 385, 1973
Fan Z., de Grijs R., Zhou X., 2010, ApJ, 725, 200
Fan Z., Huang Y.-F., Li J.-Z., Zhou X., Ma J., Wu H., Zhang T.-M., Zhao Y.-H., 2011, Res. Astron. Astrophys., 11, 1298
Federici L., Cacciari C., Bellazzini M., Fusi Pecci F., Galleti S., Perina S., 2012, A&A, 544, A155
Forbes D. A., Spitler L. R., Strader J., Romanowsky A. J., Brodie J. P., Foster C., 2011, MNRAS, 413, 2943
Forte J. C., Vega E. I., Faifer F., 2012, MNRAS, 421, 635
Fusi Pecci F., Bellazzini M., Buzzoni A., De Simone E., Federici L., Galleti S., 2005, AJ, 130, 554
Galleti S., Federici L., Bellazzini M., Fusi Pecci F., Macrina S., 2004, A&A, 416, 917
Galleti S., Bellazzini M., Buzzoni A., Federici L., Fusi Pecci F., 2009, A&A, 508, 1285
Georgiev I. Y., Goudfrooij P., Puzia T. H., 2012, MNRAS, 420, 1317
Harris W. E., 1996, AJ, 112, 1487
Huchra J. P., Brodie J. P., Kent S. M., 1991, ApJ, 370, 495
Huxor A. P., Tanvir N. R., Irwin M. J., Ibata R., Collett J. L., Ferguson A. M. N., Bridges T., Lewis G. F., 2005, MNRAS, 360, 1007
Huxor A. P., Tanvir N. R., Ferguson A. M. N., Irwin M. J., Ibata R. A., Bridges T., Lewis G. F., 2008, MNRAS, 385, 1989 (Hux08)
Huxor A., Ferguson A. M. N., Barker M. K., Tanvir N. R., Irwin M. J., Chapman S. C., Ibata R., Lewis G., 2009, ApJ, 698, L77
Huxor A. P. et al., 2011, MNRAS, 414, 770 (Hux11)
Hwang N., Lee M. G., Lee J. C., Park W.-K., Park H. S., Kim S. C., Park J.-H., 2011, ApJ, 738, 58
Ibata R., Martin N. F., Irwin M., Chapman S., Ferguson A. M. N., Lewis G. F., McConnachie A. W., 2007, ApJ, 671, 1591
Ibata R. A. et al., 2014, ApJ, 780, 128
Kim S. C. et al., 2007, AJ, 134, 706
King I., 1962, AJ, 67, 471
Kroupa P., 2001, MNRAS, 322, 231
Law D. R., Majewski S. R., 2010, ApJ, 718, 1128
Lewis G. F. et al., 2013, ApJ, 763, 4
Ma J., 2012, Res. Astron. Astrophys., 12, 115
McConnachie A. W., Irwin M. J., Ferguson A. M. N., Ibata R. A., Lewis G. F., Tanvir N., 2005, MNRAS, 356, 979
McConnachie A. W. et al., 2008, ApJ, 688, 1009
McConnachie A. W. et al., 2009, Nature, 461, 66
Mackey A. D., Gilmore G. F., 2004, MNRAS, 355, 504
Mackey A. D., van den Bergh S., 2005, MNRAS, 360, 631
Mackey A. D. et al., 2006, ApJ, 653, L105
Mackey A. D. et al., 2007, ApJ, 655, L85
Mackey A. D. et al., 2010a, MNRAS, 401, 533
Mackey A. D. et al., 2010b, ApJ, 717, L11
Mackey A. D. et al., 2013a, MNRAS, 429, 281
Mackey A. D. et al., 2013b, ApJ, 770, L17
Marigo P., Girardi L., Bressan A., Groenewegen M. A. T., Silva L., Granato G. L., 2008, A&A, 482, 883
Marín-Franch A. et al., 2009, ApJ, 694, 1498
Martin N. F., Ibata R. A., Irwin M. J., Chapman S., Lewis G. F., Ferguson A. M. N., Tanvir N., McConnachie A. W., 2006, MNRAS, 371, 1983
Martin N. F., Ibata R. A., McConnachie A. W., Mackey A. D., Ferguson A. M. N., Irwin M. J., Lewis G. F., Fardal M. A., 2013, ApJ, 776, 80
Peacock M. B., Maccarone T. J., Waters C. Z., Kundu A., Zepf S. E., Knigge C., Zurek D. R., 2009, MNRAS, 392, L55
Peacock M. B., Maccarone T. J., Knigge C., Kundu A., Waters C. Z., Zepf S. E., Zurek D. R., 2010, MNRAS, 402, 803
Perina S., Federici L., Bellazzini M., Cacciari C., Fusi Pecci F., Galleti S., 2009, A&A, 507, 1375
Perina S., Galleti S., Fusi Pecci F., Bellazzini M., Federici L., Buzzoni A., 2011, A&A, 531, 155
Perina S., Bellazzini M., Buzzoni A., Cacciari C., Federici L., Fusi Pecci F., Galleti S., 2012, A&A, 546, A31
Perrett K. M., Bridges T. J., Hanes D. A., Irwin M. J., Brodie J. P., Carter D., Huchra J. P., Watson F. G., 2002, AJ, 123, 2490
Schlafly E. F., Finkbeiner D. P., 2011, ApJ, 737, 103
Schlegel D. J., Finkbeiner D. P., Davis M., 1998, ApJ, 500, 525
Searle L., Zinn R., 1978, ApJ, 225, 357
Tanvir N. R. et al., 2012, MNRAS, 422, 162
Veljanoski J. et al., 2013a, ApJ, 768, L33
Veljanoski J. et al., 2013b, MNRAS, 435, 3654
Veljanoski J. et al., 2014, MNRAS, submitted
Wang S., Ma J., 2012, AJ, 143, 132
Wang S., Ma J., 2013, AJ, 146, 20

This paper has been typeset from a TEX/LATEX file prepared by the author.